

Steady Warps: Linear, Nonlinear, and Breaking

JIARU LI  ¹ AND YORAM LITHWICK  ^{1, 2}

¹Center for Interdisciplinary Exploration and Research in Astrophysics (CIERA), Northwestern University, 1800 Sherman Ave, Evanston, IL 60201, USA

²Department of Physics and Astronomy, Northwestern University, 2145 Sheridan Rd, Evanston, IL 60208, USA

ABSTRACT

An increasing number of protoplanetary disks shows observational signatures of warps and misalignments, raising questions of how disks sustain coherent warps and how they may break into misaligned pieces. We study the steady-state structures and breaking conditions of warped disks. To focus on the hydrodynamics, while remaining agnostic about what forces the warp, we adopt a simple but physically motivated setup: rather than including an explicit perturber or external torque, we fix the disk inclination angles β_{in} and β_{out} at the inner and outer boundaries. The disk is hence constrained to accommodate a warp between the boundaries. By varying the boundary misalignment $|\beta_{\text{out}} - \beta_{\text{in}}|$, we can explore the linear regime, the nonlinear regime, and the onset of breaking, while having good control over the warp amplitude. Combining this model with analytical theories and three-dimensional hydrodynamic simulations, we carry out a clean and systematic investigation of the hydrodynamic behaviors of warped disks. We find that, with small warps, disks settle into warp steady states that are well described by the linear theory. Moderately warped disks enter the nonlinear regime, showing several distinct features such as torque saturation, vertical “bouncing” motion of gas, and enhanced mass accretion rates. Measurements of these effects in our simulations show good quantitative agreement with nonlinear theories. Strongly warped disks are unstable: these disks are susceptible to a runaway growth of warp amplitude that ultimately leads to disk breaking. This instability may be caused by the nonlinear saturation of the disk internal torque, which occurs roughly when the warp amplitude exceeds a critical value $|\psi|_{\text{crit}} \simeq 2\sqrt{\alpha}$ for Keplerian disks.

1. INTRODUCTION

Accretion disks are not always flat; gas circulating the same central object at different radii may have different orbital inclinations, producing warped structures.

Recent observations have found an increasing amount of evidence that such warps commonly exist in protoplanetary disks. In near-infrared scattered light images, many disks exhibit non-axisymmetric dark regions (e.g., Marino et al. 2015; Stolker et al. 2017; Benisty et al. 2018; Casassus et al. 2018; Muro-Arena et al. 2020; Keppler et al. 2020; Kraus et al. 2020), which is often interpreted as shadows cast by warps (see Benisty et al. 2023). Complementary evidence comes from molecular line observations, through which several disks are found to have large-scale $m = 1$ velocity structures consistent with warped or non-planar gas flows (e.g., Panić et al. 2010; Pineda et al. 2014; Casassus et al. 2015; Winter et al. 2025). In addition, increasingly many systems have been revealed to host both warps and multiple misaligned disk components, pointing to a rich dynamical history involving both disk bending and breaking (e.g., Kraus et al. 2020; Muro-Arena et al. 2020; Bohn et al.

2022). Together, these observations raise two fundamental questions: how do disks bend and sustain coherent warps, and under what circumstances do they break into misaligned components?

Theories of warped disks have been developed over the past several decades (see, e.g., Nixon & King 2016, for an overview). In these studies, a warp is formally defined as the radial derivative of the disk inclination. Misaligned disk annuli can exert internal torques on each other (due to pressure, etc), which in turn drives the changes of the inclination profiles of the whole disk.

For nearly-Keplerian disks, how warp evolves depends on the viscous parameter α (Shakura & Sunyaev 1973) relative to the disk aspect ratio $h \equiv H/R$. Linear theories show that, for $\alpha \lesssim h$, warps can propagate as bending waves at approximately half of the sound speed, while being viscously damped at a rate $\sim \alpha\Omega$, where Ω is the angular velocity of the gas (Papaloizou & Lin 1995; Lubow & Ogilvie 2000). When $\alpha \gtrsim h$, viscous damping becomes strong enough to suppress wave propagation, so the warp instead evolves in a diffusive manner (Papaloizou & Pringle 1983). As a result, in the absence of external torques, free warps tend to flatten on the in-

termediate timescale between the orbital period $\sim \Omega^{-1}$ and the global viscous timescale $\sim (\alpha h^2 \Omega)^{-1}$.

Warps in forced disks, on the other hand, may settle into steady states on the intermediate timescale if the relevant forcing acts more slowly (e.g., Lubow & Ogilvie 2000; Foucart & Lai 2014). Note that, if α is negligible, the evolution becomes sensitive to the difference between orbital and epicyclic frequencies (i.e., the non-Keplerianity, see e.g., Ogilvie 1999, or Section 2). Hydrodynamic simulations have found good agreement with these linear theories (e.g., Lodato & Pringle 2007; Lodato & Price 2010; Kimmig & Dullemond 2024; Fairbairn 2025).

The nonlinear regime, where warp amplitudes are large, is more complex and less well understood. Analytical theories predict several important nonlinear effects, such as modifications of the internal torques (Ogilvie 1999; Ogilvie & Latter 2013a; Dullemond et al. 2022), changes to the mass accretion flow (e.g., Pringle 1992; Ogilvie 1999), and the so-called “bouncing effect”, in which gas elements would perform rapid vertical compression and expansion as they orbit around the star (Ogilvie & Latter 2013a; Fairbairn & Ogilvie 2021a,b; Held & Ogilvie 2024). These features have been identified in several numerical simulations (e.g., Lodato & Price 2010; Sorathia et al. 2013; Deng & Ogilvie 2022; Kaaz et al. 2023, 2025; Kimmig & Dullemond 2024). In low- α disks, wave coupling can also lead to parametric instability (Gammie et al. 2000; Ogilvie & Latter 2013b), which was not seen in the early numerical studies but emerged in recent high-resolution simulations (e.g., Paardekooper & Ogilvie 2019; Deng et al. 2021; Deng & Ogilvie 2022; Fairbairn & Stone 2025). Due to the complex nature of nonlinear hydrodynamics, recent studies tend to either pursue more powerful simulations (e.g., Deng & Ogilvie 2022; Kaaz et al. 2025) or develop alternative frameworks, such as affine models (Ogilvie 2018) and ring models (Fairbairn & Ogilvie 2021a).

Extreme nonlinear evolution can lead to disk breaking, where the disk splits into multiple disconnected planes (e.g., Larwood et al. 1996; Nixon et al. 2012, 2013; Zhu 2019; Liska et al. 2021). Several theories have been proposed to explain the mechanisms of breaking, including resonance with tidal forcing (Lubow & Ogilvie 2000; Martin et al. 2020), rapid nodal precession (Zhu 2019; Martin et al. 2020; Rabago et al. 2024), and linear instabilities related to the anti-diffusion of the disk density (Doğan et al. 2018; Raj et al. 2021). Yet a general condition and physical mechanisms that trigger disk breaking remain unclear.

In this paper, we focus on the long-lived warp steady state (WSS), the configuration in which rapid bending-wave oscillations have damped out and the disk’s inclination profile stops changing, despite the slow evolution set by the changing background surface density. Such states are more likely to be observable than their transient predecessors: given the lifetimes of protoplanetary disks, any warps present are likely to have relaxed into quasi-steady configurations. Our primary goals are to determine the WSS structures of disks, both in the linear and the nonlinear regimes, and to diagnose how a sufficiently large warp drives disk breaking.

We perform both theoretical analysis and numerical simulations. To focus on the hydrodynamics, while remaining agnostic about what forces the warp, we adopt a simple but physically motivated setup: rather than include an explicit perturber or external torque, we fix the disk inclination angles β_{in} and β_{out} at the inner and outer boundaries. The disk is hence constrained to accommodate a warp between the boundaries, and we can study the resulting steady-state structure. In the simulations, we also lower the surface density in the middle of the disk (but keep it non-empty), allowing us to localize the warp and reduce the possible influence of artificial boundary conditions. Our setup provides a clean laboratory for testing the hydrodynamic response of disks to generic perturbations. By varying the boundary misalignment $|\beta_{\text{out}} - \beta_{\text{in}}|$, we can explore the linear regime, nonlinear regime, and the onset of breaking, while having good control over the warp amplitude. As we will show, our simulations show excellent agreement with the theories.

The rest of this paper is organized as follows. We review the linear theory of warped disks in Section 2, and test the theory using hydrodynamic simulations in Sections 3. In Section 4, we extend the theory in nonlinear regime, allowing us to estimate the maximum mutual inclination $|\beta_{\text{out}} - \beta_{\text{in}}|$ for which a disk can sustain a continuous warp. We then perform hydrodynamics simulation in Section 5 to analyze the nonlinear behaviors and the breaking process of disks when $|\beta_{\text{out}} - \beta_{\text{in}}|$ becomes large. Finally, we conclude in Section 7.

2. LINEAR THEORY

2.1. Linear Warp Equations

We focus on a disk with a steady warp (Figure 1). We imagine that the disk is forced to have unequal inclinations at its inner and outer boundaries, and study the resulting inclination profile in between. As discussed above, the timescale for the disk’s inclination to reach its steady profile is much shorter than the disk’s viscous time, and so in this section we regard the surface den-

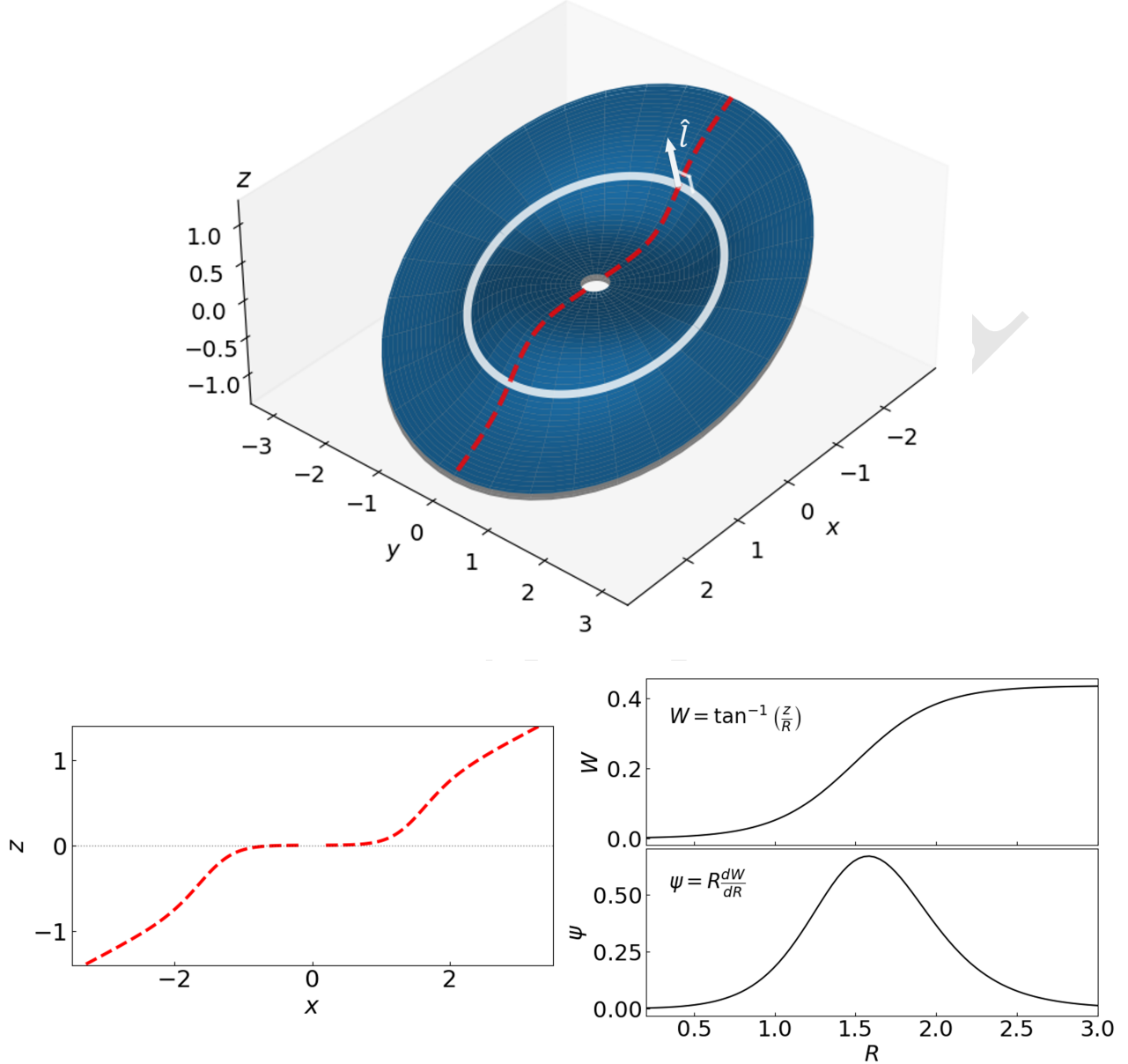


Figure 1. Midplane of a warped disk. This disk has no twist (W is purely real). **Left:** 3D diagram of the disk. The red dashed curve marks the maximum $|z|$ at each R , which lies along $y = 0$ for this untwisted disk. The white circle marks the location of the disk midplane at $r = 1.75$, while the arrow represents the direction of the tilting vector \hat{l} at this radius. **Right Top:** Same as red-dashed curve in left panel. **Right Bottom:** Inclination and warp.

sity profile as an arbitrary time-independent function of radius.

The equations for the inclination have been derived many times (Pringle 1992; Ogilvie 1999; Fairbairn 2025, etc.). We derive them again in Appendix A, because our assumption of a steady warp facilitates a conceptually simpler derivation, and allows us to proceed from first principles. Our derivation also makes clear that the resulting steady equations are equally valid whether $\alpha < h$ or $\alpha > h$, i.e., in the “wave-like” or “diffusive”

regimes. Here we summarize the derivation, highlighting the physical interpretation.

We adopt cylindrical coordinates (R, ϕ, z) , a globally isothermal equation of state, and an α viscosity. We first solve for an unperturbed disk that is axisymmetric and aligned with the z axis. We then perturb the equations of motion to linear order, and assume that perturbed variables take on an $m = 1$ dependence in ϕ , and that their dependence on z is the leading term in a Hermite expansion. Higher-order Hermite terms,

which have smaller vertical wavelengths, are suppressed by powers of the disk aspect ratio

$$h \equiv H/R \quad (1)$$

where H is the scale height. The resulting linear equations of motion, which we call the linear warp equations, are

$$\frac{d}{dR}(\sigma u_r) = 0, \quad (2)$$

$$(2\alpha + i\epsilon) u_r = R \frac{dW}{dR}, \quad (3)$$

which describe in the warp structure in terms of two variables, W and u_r ; we will discuss their physical meaning shortly. Here, σ is a scaled surface density, which is related to the true surface density Σ via

$$\sigma \equiv \frac{1}{2} \Sigma H^2 R^2 \Omega^2, \quad (4)$$

and ϵ quantifies the deviation of the epicyclic frequency from its Keplerian value. The expression for ϵ is given by Equation (A13); it is typically small ($O(h^2)$), but can become big if $d\Sigma/dR$ is big. Rayleigh stability necessitates $\epsilon > -1$.

The variables W and u_r have direct physical interpretations. The former is the complex inclination. In other words, the disk's unit normal $\hat{\mathbf{l}}$ is, in Cartesian $[x, y, z]$ components

$$\hat{\mathbf{l}} \approx [\text{Re}(W), \text{Im}(W), 1] \quad (5)$$

to linear order in W .¹ Figure 1 (left panel) depicts the midplane of a warped disk with purely real W , meaning that it is not twisted. In this case, the maximum height at each radius lies at $y = 0$, as depicted by the dashed red line, which is repeated in the top right panel. The lower-right panels show the W profile, which in this case of real W is the usual (real-valued) inclination, and its warp ψ . For general complex W , the complex-valued warp is defined as

$$\psi \equiv \frac{dW}{d \ln R}. \quad (6)$$

In the figure, the warp is concentrated around $R \sim 1.5$. At much smaller or bigger R , the disk is unwarped, meaning that the midplane is a flat plate, in which the inclination W is constant.

¹ In what follows, we shall define $\hat{\mathbf{l}}$ more precisely, as the unit vector that is in the direction of the angular momentum of a spherical shell. See Equation (C72) in the Appendix C.1 for the full definition. We also show in that appendix that the resulting $\hat{\mathbf{l}}$ is given by Equation (5), to linear order in W , after dropping $\mathcal{O}(hW)$ and $\mathcal{O}(h^2\psi/(2\alpha + i\epsilon))$ corrections.

The variable u_r quantifies sloshing motions that are in the “disk-horizontal” direction, i.e., perpendicular to $\hat{\mathbf{l}}$. As shown in Appendix A.3, the radial speed in the (spherical) $\hat{\mathbf{r}}$ direction is

$$\frac{v'_r}{\Omega R} = u_r \frac{z}{R} e^{-i\phi'}, \quad (7)$$

where u_r has an amplitude $\sim v'_r/c_s$ at $z = H$ (after dropping $O(h^2)$ corrections). The dependence on z in Equation (7) indicates sloshing, in that the nearly-horizontal motion has an antisymmetric profile in z .²

We turn now to the interpretation of Equation (3) (Equation 2 will be considered shortly), which states that the warp ψ drives sloshing. The dynamics may be appreciated by considering two neighboring circular rings in the midplane of a warped disk. Since their orbit normals $\hat{\mathbf{l}}$ differ, from the perspective of one ring its neighbor moves up and down. That causes a disk-horizontal pressure gradient, which in turn forces the sloshing (see, e.g., discussion in Ogilvie & Latter 2013a, and their Figure 5). Equation (3) shows that for a given warp, the sloshing is $\propto 1/(2\alpha + i\epsilon)$, which is almost always very large in magnitude. The reason for this extreme reaction is that the vertical motions that accompany the warp are nearly resonant with free sloshing (epicyclic-type) motions in a nearly Keplerian disk (e.g., Papaloizou & Pringle 1983; Ogilvie 1999).

It will prove useful to re-express the linear warp equations in terms of

$$G \equiv -\sigma u_r, \quad (8)$$

which we show in Section 4.1 represents the torque. The equations then become

$$\frac{dG}{dR} = 0, \quad (9)$$

$$(2\alpha + i\epsilon) G = -\sigma R \frac{dW}{dR}. \quad (10)$$

The physical interpretation of the first linear equation is now apparent, i.e., the rate at which angular momentum crosses a cylinder of radius R (the torque) must be independent of R in WSS, or else the angular momentum would accumulate.

² The reason v'_r rather than v'_R is relevant for sloshing may be appreciated by considering an unwarped disk (a flat plate) that is inclined relative to the $z = 0$ plane. In that case, $v'_r = 0$ as it is for an uninclined plate. But $v'_R \neq 0$ because inclining the disk introduces velocities in the R -direction that have the same z and ϕ -dependence as Equations (A21) to (A23). Note we define the amplitude u_r in Equation (7) with z/R instead of z/H so $u_r \sim v'_r/c_s$.

2.2. Linear Solutions

The first linear equation (Equation 9) has solution $G = \text{const}$. The second can then be integrated for the $W(R)$ profile, given $\sigma(R)$. The boundary conditions are subtler. If the disk is not subject to external forcing, then $G = 0$ at the boundaries, and the steady solution is trivial, $W = \text{const}$, i.e., the disk is a flat plate, with constant inclination. On the other hand, an external perturber such as a planet or the outer disk can apply a torque, forcing G . The details depend on the perturber. But since we are interested in the disk's inclination profile rather than its interaction with a perturber, we adopt an equivalent, but conceptually slightly different, approach: we fix the inner and outer inclinations, and solve for $W(R)$ in between. Equation (10) gives

$$R \frac{dW}{dR} = \text{const} \frac{2\alpha + i\epsilon}{\sigma}, \quad (11)$$

where the right-hand side is a known function of R . Without loss of generality, we choose $W = 0$ at the inner boundary, and $W = 1$ at the outer. The latter is general because the problem is linear, and so $W(R)$ scales in proportion to its value at the outer boundary. Equation (11) is then integrated, with the constant in the equation adjusted to match the outer inclination.

Equation (11) shows that the warp is largest where the scaled surface density σ is smallest (ignoring ϵ for now). Intuitively, a smaller surface density means that the disk is weaker, and the disk bends primarily where it is weakest. Figure 2 shows some solutions of the linear equations with three different assumed surface density profiles, which are shown in the top-left panel. We set the domain to be

$$0.5 < R < 3 \quad (12)$$

and

$$\alpha = 0.019, \quad (13)$$

$$h = 0.02 \times R^{1/2}, \quad (14)$$

where the latter is needed to obtain ϵ . The green Σ profile is a power law, $\Sigma \propto R^{-3/2}$. The resulting W and ψ are shown in the right panels. For this case, the warp $|\psi|$ is dominated at the inner boundary. In general, a power-law Σ profile produces a warp that is largest at the boundary.

For the other two Σ profiles, we impose gaps of depth 0.2 and 0.05. As a result, the warp is concentrated in the gap, as may be seen in the right panels. For our later comparisons, it will prove convenient to keep the warp away from the domain boundaries, so that it is not affected by uncertain boundary conditions. We will do

that by imposing a gap. But imposing a gap introduces a small complication: ϵ can get large at gap edges, as shown in the lower-left panel. Nonetheless, as long as $|\epsilon| \ll |\alpha|$, as is true within most of the gap for the profiles shown, the effect of ϵ may be ignored there.

3. LINEAR WARP SIMULATION

3.1. Setup

We perform 3D hydrodynamics simulations of warped disks using Athena++ (Stone et al. 2020) to study the behavior of disks at different warp amplitudes. The simulations solve the Navier-Stokes equations for a globally isothermal viscous disk in spherical polar coordinates (r, θ, ϕ) . Their setup is based on the setup studied in Section 2. The initial surface density profile is the same as the black curve in Figure 2, with a gap in the central region. The disk is then evolved while holding the inner inclination at zero, and the outer inclination at a fixed value (β_{out}). Table 1 lists the main simulation parameters. The time unit is chosen so that the Keplerian angular frequency at $r = 1$ is unity. Boundary conditions fix the inner and outer inclinations by fixing the value of Σ at the outer boundary throughout the course of the simulation. They also model an inward mass flux through the inner boundary (Appendix D.1).

In this section, we study the time evolution of a small warp, with simulation C03init. This simulation is distinguished from the others in that the initial inclination profile is set arbitrarily, rather than to the solution of the linearized equation.

3.2. Warp Profile

Table 1. Simulation parameters. The upper table lists parameter values that are common to all runs. The lower table summarizes run-specific parameters: the outer inclination β_{out} , the half-width of the domain in θ , and the number of grid points.

	c_s	α	r -domain
	0.02	0.019	$(0.5, 3.0)$
Name	β_{out}	half-width in θ	(N_r, N_θ, N_ϕ)
C03init	0.033	0.24	$(256, 256, 260)$
C10	0.10	0.74	$(256, 728, 260)$
C15	0.15	"	"
C20	0.20	"	"
C30	0.30	"	"
C40	0.40	"	"

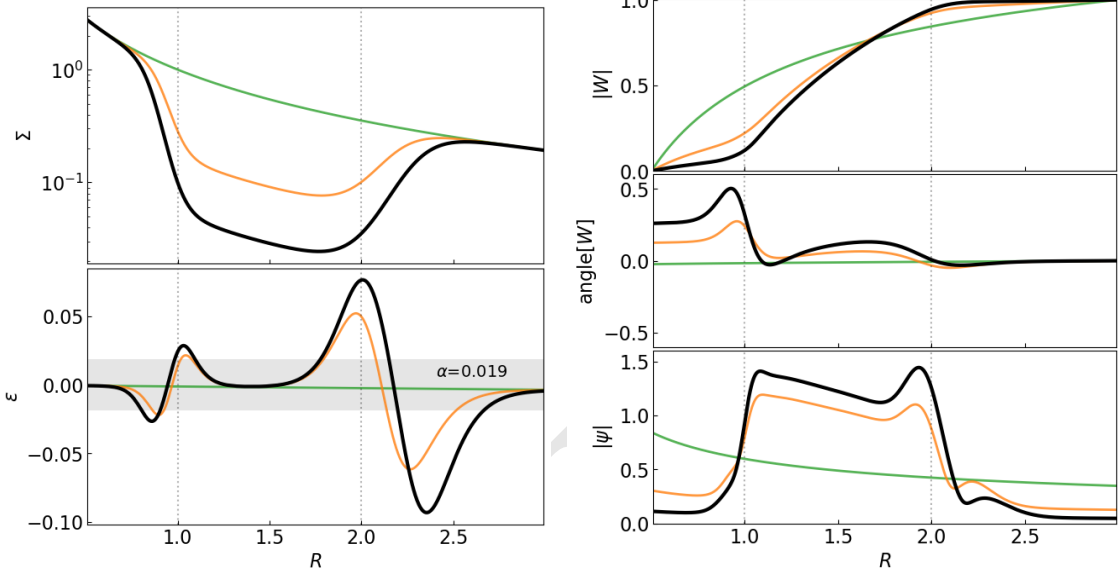


Figure 2. Examples WSS structures for disks with different background profiles. **Upper left:** Background surface density profiles of Σ , with gap edges marked with vertical dotted lines. **Lower left:** Background ϵ profiles calculated based on Σ ; all disks adopts $\alpha = 0.19$, with the gray-shaded region shows where $|\epsilon| < \alpha$. **Top Right:** Steady-state $|W|$ profiles calculated from the linear steady-state Equations (2) and (3). **Middle Right:** Phase angle of the steady-state complex W . **Bottom Right:** Warp amplitude $|\psi|$ based on the $|W|$ profiles. We take the **thick black** case as our fiducial model.

Our main diagnostics are the angle-averaged surface density

$$\Sigma = \frac{1}{2\pi r} \int \rho dS \quad (15)$$

and the average specific angular momentum

$$\ell = \frac{1}{2\pi r \Sigma} \int \rho \mathbf{r} \times \mathbf{v} dS \quad (16)$$

where $dS \equiv r^2 \sin \theta d\theta d\phi$; both Σ and ℓ are all functions of r and t . From \mathbf{h} , we define the unit vector

$$\hat{\mathbf{l}} = \ell / |\ell|, \quad (17)$$

and thence angles β and γ via

$$\hat{\mathbf{l}} = [\sin \beta \cos \gamma, \sin \beta \sin \gamma, \cos \beta], \quad (18)$$

where β is the inclination, and $\gamma - \pi/2$ is the longitude of ascending node. We also define the vectorial warp as

$$\psi = \frac{d\hat{\mathbf{l}}}{d \ln r} \quad (19)$$

(Ogilvie 1999; Dullemond et al. 2022), which lies in the plane of the disk ($\psi \cdot \hat{\mathbf{l}} = 0$).

As we show in Appendix C, the vectors $\hat{\mathbf{l}}$ and ψ are closely related to the complex variables W and ψ used in Section 2:

$$W \approx \hat{\mathbf{l}} \cdot \hat{\mathbf{x}} + i \hat{\mathbf{l}} \cdot \hat{\mathbf{y}} \approx \beta e^{i\gamma} \quad (20)$$

$$\psi \approx \psi_x + i\psi_y \quad (21)$$

where the unit vectors $\hat{\mathbf{x}}$ and $\hat{\mathbf{y}}$ are relative to the global simulation frame, and $\psi_x \equiv \psi \cdot \hat{\mathbf{x}}$, and similarly $\psi_y \equiv \psi \cdot \hat{\mathbf{y}}$.

The vectors $\hat{\mathbf{l}}$ and ψ are in general preferable to their complex counterparts because their definitions are independent of the coordinate system, and thus apply even when the warp is nonlinear. The complex numbers should be regarded as approximate coordinate-dependent representations of the vectors. Nonetheless, they remain useful because they allow for a simple expression of linear theory.³

For the simulation studied in this section (C03init), the initial inclination profile rises linearly across the domain, from $\beta = 0$ to 0.033, with no twist ($\gamma = 0$). Snapshots of Σ and inclination-related variables at two subsequent times are shown in Figure 3.

The evolution of Σ (panel a) is virtually unaffected by the warp in this run, as we have confirmed by comparing with a zero-inclination disk. The viscous time across a distance r is $t_{\text{vis}} \approx \alpha^{-1} h^{-2} r^{3/2} \approx 10^5 r^{1/2}$. The evolution timescale of Σ seen in Figure 3(a) is faster than

³ We emphasize that our notational convention is that ψ represents the complex variable, and ψ represents the vector, and ψ should never be confused with the magnitude of ψ , which we denote $|\psi|$. We shall apply the same convention to complex variable G , defined in Equation (8), and its vectorial counterpart \mathbf{G} , which is defined below (Equation 24); and also to complex variable u_r and vector \mathbf{u}_r .

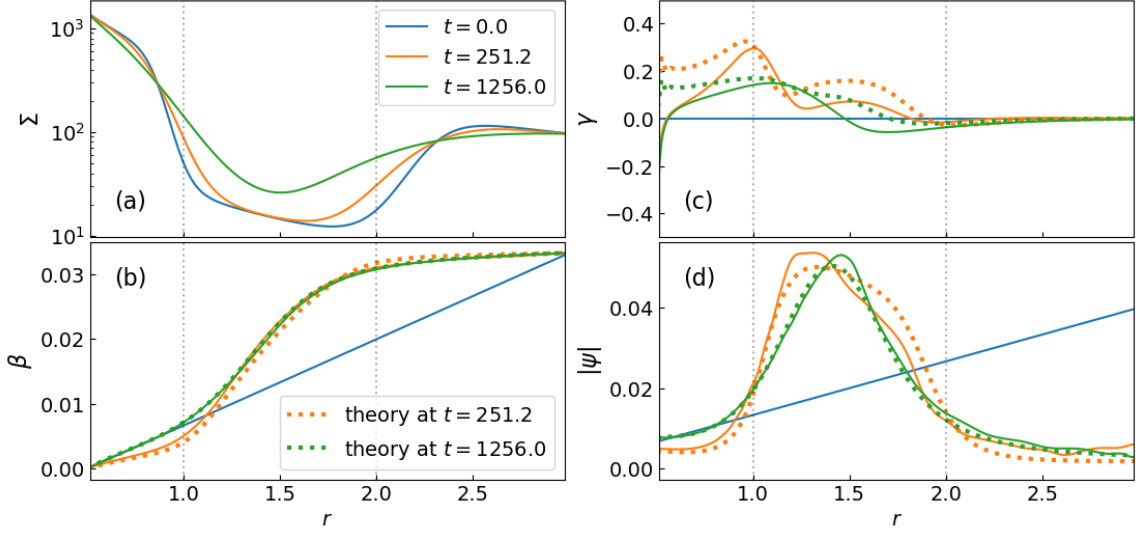


Figure 3. Structure evolution of a weakly warped disk with $\beta_{\text{out}} = 0.033$. The solid-colored curves show the surface density Σ (measured using Equation 15), disk orbital inclination angle β , phase γ (Equation 18) and warp amplitude $|\psi|$ (Equations 19) at different times. The dotted curves shows the linear steady-state solution based on real-time Σ and ϵ profile.

that by a factor of around 100, due to the narrowness of the gap edges.

The time for the inclination to reach its steady profile is much shorter than the evolution time of Σ . There are two relevant warp timescales, one associated with the time for a warp to travel $t_{\text{warp},c_s} \approx (2r/c_s) = 100r$, and the other for the warp to damp $t_{\text{warp},\alpha} \approx \alpha^{-1}r^{3/2} = 52r^{3/2}$. Figure 4 shows the time evolution of β at the middle of the gap. The initial evolution exhibits a damped oscillation, on a timescale of ~ 100 , in agreement with the two warp timescales. After that, the inclination evolves much more slowly, on the viscous timescale of Σ , suggesting that the disk is in WSS. Therefore beyond a time of ~ 100 , the steady warp theory (Section 2) should be applicable.

Figure 3(b) shows snapshots of the inclination profile as solid curves, and the theoretical prediction as dotted curves, which is obtained by integrating Equation (11) with the real-time Σ and ϵ and setting $\beta = |W|$. The theory is seen to agree well with the simulations.

Panel (c) is the same as (b), except showing the γ profile. The agreement between measured and predicted γ is adequate, although worse than for β . In linear theory, γ differs from zero due to the effect of non-Keplerianity (ϵ), as may be seen from the integral of Equation 11, and recalling that $\angle W \approx \gamma$. Thus, the mismatch in panel (c) is likely due to an insufficiently accurate evaluation of ϵ as the density evolves in time. But since γ has a sub-dominant effect on the warp $|\psi|$, the agreement in panel (c) is not too concerning.

Panel (d) shows the warp profile (Equation 19), demonstrating good agreement with linear theory.

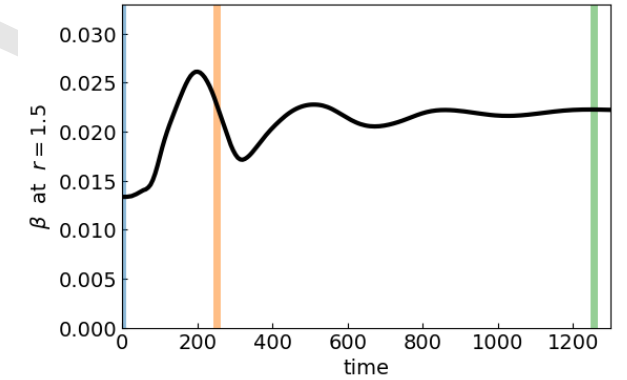


Figure 4. Time evolution the disk inclination β at $r = 1.5$ in the simulation shown in Figure 3 (C03init, $\beta_{\text{out}} = 0.033$). The colored vertical lines mark the time of the snapshots shown in Figure 3.

3.3. Vertical and Azimuthal Structure: ρ and v_r

Figure 5 shows the density and radial velocity fields on a spherical shell in the middle of the gap ($r = 1.5$), at time $t = 251.2$. The left panels show those fields as a function of the angular variables used in the Athena++ simulation, i.e., in the global frame in which the inner disk has zero inclination. Because the disk has non-zero inclination at $r = 1.5$, the fields are dominated by a half-sinusoidal variation in ϕ , i.e., they are proportional to $\cos(m\phi)$ with $m = 1$. To remove that trivial variation, in the right panel we rotate the coordinate system to one in which $\hat{\ell}$ is vertical, as detailed in the caption. The rotated ρ is nearly the same as an unperturbed flat disk. But there is a faint hint of an $m = 2$ pattern, due to nonlinear bouncing (Section 5.2). The rotated

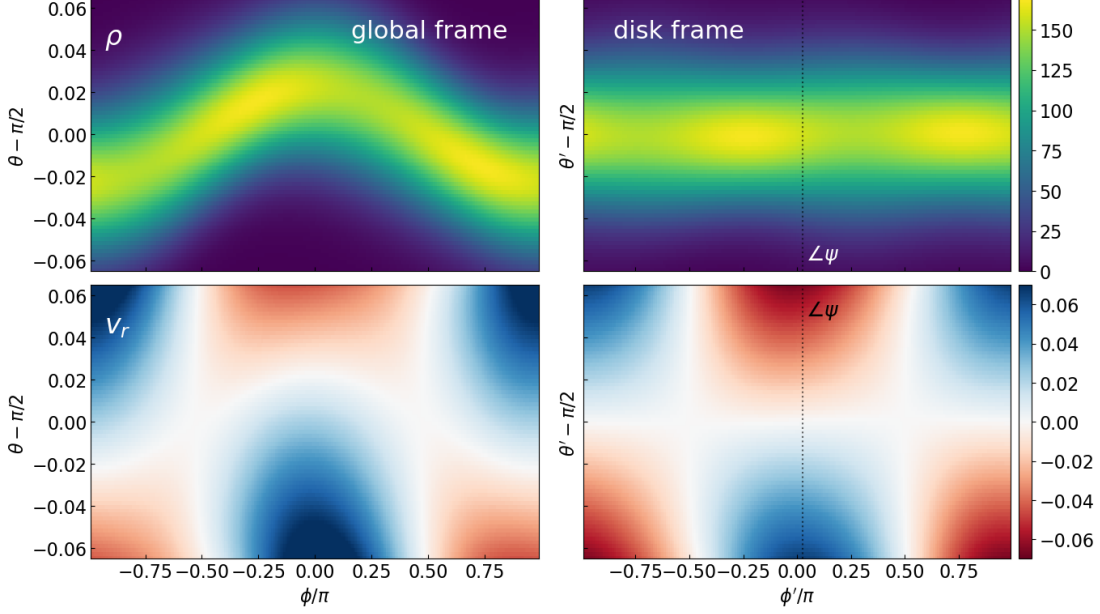


Figure 5. Density (top row) and radial velocity field (bottom row) at $r = 1.5$ for the C03init simulation at $t = 251.2$. The left panels show the quantities in the simulation coordinates, while the right panels show the same data transformed into the local disk frame where the disk midplane is placed at $\theta = \pi/2$. Specifically, we plot on the right the fields of $\rho(\mathbf{r}')$ and $v_r(\mathbf{r}')$ with $\mathbf{r}' = R_y(\beta)R_z(\gamma)\mathbf{r}$, where \mathbf{r} is the position vector in the unrotated simulation frame and R_y and R_z are the rotational matrices around the $\hat{\mathbf{y}}$ and $\hat{\mathbf{z}}$ axis. The vertical dotted lines mark the ϕ angle where ψ is pointing.

radial velocity field exhibits the key linear effect: sloshing. As described above, sloshing is driven by the warp; see Equation (3), in which u_r represents sloshing and RdW/dR the warp. In the lower-right panel of Figure 5 we show a vertical line labeled $\angle\psi$ that marks the direction of the warp vector ψ . Note that ψ is perpendicular to $\hat{\mathbf{l}}$, and so lies inside the disk orbital plane. As shown by Equation (3), the phase of u_r is the same as that of the warp when $|\epsilon| \ll 2\alpha$. This is confirmed by Figure 5, where $\angle\psi$ is nearly the same as the peak in radial velocity, because ϵ is negligibly small in the middle of the gap.

4. NONLINEAR THEORY

While the linear theory accurately describes small-amplitude warps, as we have shown in the last Section, it fails as the warp amplitude ψ increases. In this Section, we extend the theory to the nonlinear regime by examining how sloshing couples to the global evolution of the disks angular momentum.

4.1. Internal Torque \mathbf{G}

The global evolution of a disk's tilt is governed by the conservation of angular momentum:

$$\partial_t (\mathcal{M}\ell) + \partial_r \mathbf{F}_L = 0, \quad (22)$$

where $\mathcal{M} \equiv 2\pi r\Sigma$ is the radial density of the disk and ℓ is averaged specific angular momentum vector (Equa-

tion (16)). The \mathbf{F}_L term represents the radial flux of angular momentum,

$$\mathbf{F}_L = \int \rho v_r (\mathbf{r} \times \mathbf{v}) dS + \mathbf{F}_\nu, \quad (23)$$

including both a material term and a viscous term \mathbf{F}_ν . To focus on the warp dynamics, we define the *internal* torque \mathbf{G} as

$$\mathbf{G} \equiv \mathbf{F}_L - \dot{M}\ell, \quad (24)$$

where

$$\dot{M} \equiv \int v_r \rho dS \quad (25)$$

is the radial flux of mass. On the right-hand side, we subtract from \mathbf{F}_L by the angular momentum flux due to mass accretion flow; the resulting \mathbf{G} includes only the internal portion of the torque (i.e., Reynolds stresses and viscous torque).⁴

In a warp steady state, the disk's tilt $\hat{\mathbf{l}}$ remain fixed ($\partial_t \hat{\mathbf{l}} = 0$ and $\partial_t (\mathcal{M}\ell) \propto \hat{\mathbf{l}}$), implying that the internal

⁴ We follow the literature in calling \mathbf{G} the torque. Our definition is same as Equation (52) in Ogilvie & Latter (2013a) and Equation (C.5) in Kimmig & Dullemond (2024). It is also equivalent to the flux F defined by Equation (29) in Papaloizou & Terquem (1995), excepted that we included the viscous effect. Lubow & Ogilvie (2000) also defined their internal torque as G , but with a prefactor of $1/(2\pi)$.

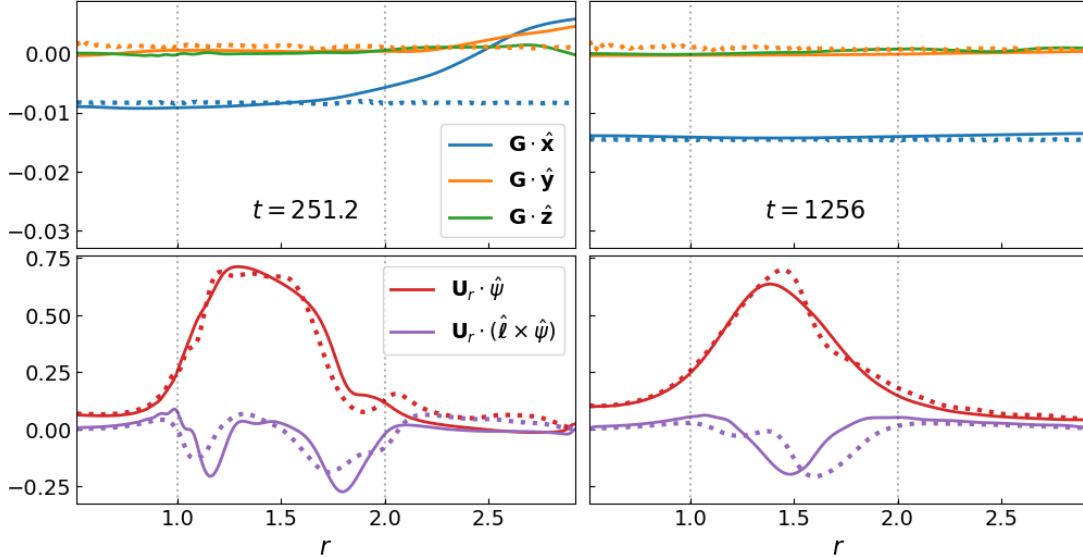


Figure 6. Internal torque \mathbf{G} and the sloshing vector \mathbf{u}_r in the C03init simulation. The upper panel shows the $\hat{x}\text{-}\hat{y}\text{-}\hat{z}$ components of \mathbf{G} (Equation 24). The lower panel shows the two components of \mathbf{U}_r (Equation 38). The dotted curves show the linear theory predictions (Equations 28, and 35 to 38) based on real-time Σ and ϵ profile.

torque must satisfy

$$(\partial_r \mathbf{F}_L)_{\perp} = 0. \quad (26)$$

We use the subscript \perp to denote components of a vector perpendicular to $\hat{\mathbf{l}}$. This condition states that the perpendicular component of the torque must vanish, otherwise the disk continues to change its orientation.

Equation (26) is the nonlinear generalization of Equations (2) and (9). In the linear regime, accretion tends to be weak; with $\hat{\mathbf{l}} \simeq \hat{\mathbf{z}}$ and the \perp components be in the $x\text{-}y$ plane, Equation (26) simplifies to

$$\partial_r G_x = 0, \quad \partial_r G_y = 0. \quad (27)$$

Inserting the parameterization of Equation (7) into the right-hand side of Equation (23) gives

$$\mathbf{G} \approx -\sigma [\text{Re}(u_r), \text{Im}(u_r), 0] \quad (28)$$

to linear order, as shown in Appendix C.2, i.e., the torque is intimately connected to sloshing (e.g., Papaloizou & Pringle 1983; Papaloizou & Terquem 1995; Ogilvie 1999). The first linear warp equation then follows immediately from Equation (27). Parenthetically, we may also now observe from Equation (28) that the previously defined complex-valued $G \equiv -\sigma u_r$ is indeed the complexified torque, i.e.,

$$G \approx G_x + iG_y \quad (29)$$

verifying the claim below Equation (8).

To illustrate the consequences of what we have derived as far, we examine the profile of \mathbf{G} in the linear simulation C03init in Figure 6, which will also set the stage

for our subsequent analysis of the nonlinear simulations. We choose to measure \mathbf{G} as

$$\mathbf{G} = \int \rho v_r (\mathbf{r} \times \mathbf{v}) dS - \dot{M} \mathbf{h} \quad (30)$$

throughout this paper. This definition is same as in Equation (24) but without the viscous term. It turns out that dropping the viscous term has very little effects on our analysis.

The top panels show the profiles of the three Cartesian components of \mathbf{G} , in the simulation's global coordinate system, along side with the theoretical predictions for G_x and G_y determined by solving the linear warp equations. The measured G_x and G_y are each nearly spatially constant; their values agree with the theoretical predictions throughout most of the domain, although in the early-time snapshot (top-left panel) it is clear that the simulation is not yet in WSS at $r \gtrsim 2$.

The green curves in Figure 6 show G_z . In apparent contradiction with Equation (28), it does not vanish. That is because G_z is primarily due to viscous accretion, i.e., the $m = 0$ component of the radial velocity, which was excluded in deriving Equation (28). This normal component of the torque is not directly relevant for the warp, but rather a result of density evolution.⁵

⁵ The torque associated with viscous accretion is perpendicular to the disk, which for an inclined disk is not purely in the $\hat{\mathbf{z}}$ direction. Thus the tilted \mathbf{T}_{vis} from viscous accretion can pollute G_x and G_y , and vice versa (Dullemond et al. 2022). In our simulations presented below, the effect of this pollution is minor.

In the nonlinear regime, Equation (27) becomes inaccurate because (1) the disk tilting vector $\hat{\mathbf{l}}$ is no longer approximately $\hat{\mathbf{z}}$ and (2) the \perp components are not in the $\hat{\mathbf{x}}$ and $\hat{\mathbf{y}}$ components. We instead argue that, regardless the direction of \mathbf{G}_\perp , the magnitude $|\mathbf{G}_\perp|$ needs to be a constant of r , i.e.,

$$\partial_r |\mathbf{G}_\perp| \simeq 0. \quad (31)$$

This equation has the similar essence as Equation (26) and (27), but is accurate only when \dot{M} and $\partial_t \hat{\mathbf{l}}$ are both small. Nevertheless, Equation (31) can still be more convenient than Equation (26) because $|\mathbf{G}_\perp|$ only depends on $|\psi|$, as we shall see later.

4.2. Sloshing \mathbf{U}

We turn now to the nonlinear generalization of the second warp equation (Equation 3), which we repeat here as

$$u_r = \frac{1}{2\alpha + i\epsilon} \psi, \quad (32)$$

in terms of complex-valued u_r and ψ . Recall that this describes the “local” part of the warp problem: how a given warp ψ drives the horizontal sloshing motion u_r , to the linear order.

The nonlinear response of the fluid has been determined by Ogilvie & Latter (2013a) using a warped shearing box. These fluid’s response in turn determines the internal torque \mathbf{G} through Equations (23). For coupling to the first warp equation which can then be coupled to the first warp equation (Equation 31 or 27), we are primarily interested in the \mathbf{G}_\perp component, which may in general be written as

$$\mathbf{G}_\perp = -\sigma (Q_2 \psi + Q_3 \hat{\mathbf{l}} \times \psi) \quad (33)$$

where Q_2 and Q_3 are nonlinear functions of $|\psi|$, α and ϵ . The theory for how to calculate the nonlinear Q_2 and Q_3 is worked out in Ogilvie (1999) and Ogilvie & Latter (2013a). Equation (33) is the nonlinear generalization of the second warp equation (10).

As a sanity check, for linear warps, the expressions for Q_2 and Q_3 may be found by combining $G_\perp = -\sigma u_r$ (where we now append subscript \perp because it represents the complexified in-plane torque) with Equation (32), which yields

$$G_\perp = -\sigma \frac{1}{2\alpha + i\epsilon} \psi. \quad (34)$$

Comparing with Equation (33) shows that for linear warps

$$Q_{2,\text{lin}} = \text{Re} \left(\frac{1}{2\alpha + i\epsilon} \right), \quad (35)$$

$$Q_{3,\text{lin}} = \text{Im} \left(\frac{1}{2\alpha + i\epsilon} \right), \quad (36)$$

where are both independent of ψ .

In the lower panels of Figure 6, we verify Equation (33) in simulation C03init. To do so, it is convenient to first define the vector

$$\mathbf{U} \equiv -\mathbf{G}_\perp / \sigma. \quad (37)$$

We can think about \mathbf{U} as approximately the (mass-averaged) dimensionless sloshing vector (see, e.g., Equation 54 of Ogilvie & Latter 2013a). For linear warps, the vector \mathbf{U} has magnitude $|u_r|$ and lies within the disk plane, pointing to where the radial velocity v_r hits its maximum above the midplane (e.g., at $\phi \approx 0$ in the lower-right panel of Figure 5). In terms of \mathbf{U} , the second warp equation becomes

$$\mathbf{U} = Q_2 \psi + Q_3 \hat{\mathbf{l}} \times \psi \quad (38)$$

The solid curves in the lower panels of Figure 6 shows the dot product of \mathbf{U} with the vectors $\hat{\psi}$ and $\hat{\mathbf{l}} \times \hat{\psi}$. The dotted curves show the linear predictions of $Q_{2,\text{lin}} |\psi|$ and $Q_{3,\text{lin}} |\psi|$ using the real-time σ profile. The simulated values agree well with the predictions.

4.3. Nonlinear Solutions

Equations (26) and (38) show that a warped disk is governed by two coupled processes: the local warp ψ drives a sloshing motion \mathbf{U} , and this sloshing generates a internal torque $\mathbf{G}_\perp = -\sigma \mathbf{U}$ that uphold the global warp profile. The steady-state structure is found by matching the global torque requirement ($\partial_r |\mathbf{G}_\perp|^2 \simeq 0$) with the local nonlinear torque-warp relation presented above.

The solutions to the two nonlinear warp equations may, to a large extent, be understood graphically. Figure 7 shows an example, for which the assumed σ profile is shown in panel (a), which corresponds to the Σ profile in Figure 3. To focus on the essence, we let $\partial_r |\mathbf{G}_\perp| = 0$; Equation 37 implies $|\mathbf{U}| \propto \text{const.}/\sigma$. Therefore, in panel (b) we plot three curves of $\text{const.}/\sigma$, with four different values of constant $|\mathbf{G}_\perp|$. Those represent possible solutions for the global $|\mathbf{U}(r)|$ profiles.

Next, given \mathbf{U} one may determine ψ by solving the second warp equation in the form of Equation (38). Panel (c) plots the local $|\mathbf{U}| = |Q_2 \psi + Q_3 \hat{\mathbf{l}} \times \psi|$ versus $|\psi|$ relation, with the Q_2 and Q_3 functions are obtained

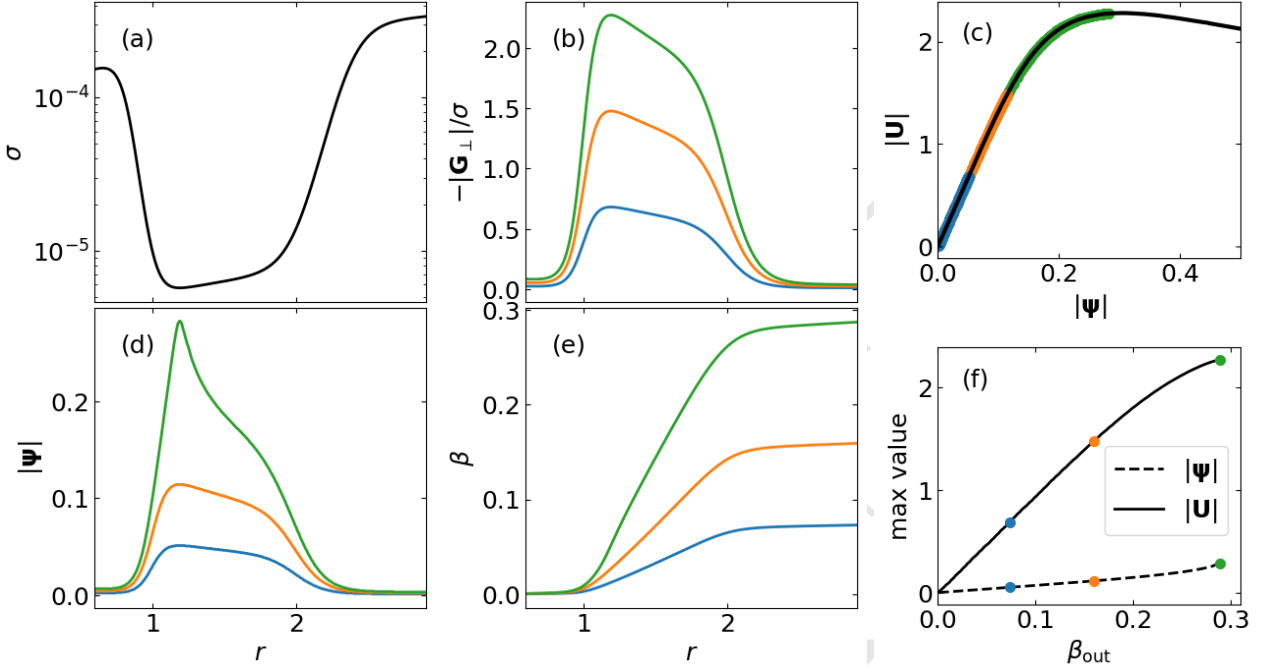


Figure 7. Example solutions to the nonlinear steady-state warp equations (31) and (33). (a) Fiducial radial profile of σ , given by Equation (4). (b) Global profiles for the sloshing amplitude $|U|$, based on the nonlinear torque Equation (31); the three colors represent solutions for different values of $|G_w| = \text{constant}$, same for the other panels. (c) Local nonlinear relation between sloshing $|U|$ and warp amplitude $|\psi|$ based on Ogilvie & Latter (2013a); the colored dots indicates the values of $|U|$ from (b). (d) Resulting $|\psi|$ profiles obtained by matching the two $|U|$'s in (b) and (c). (e) Corresponding inclination profiles β . (f) Maximum warp and sloshing amplitude, $|\psi|$ and $|U|$, as functions of boundary misalignment β_{out} ; the curve terminates at the critical β_{out} where $|\psi| = |\psi|_{\text{crit}}$.

following Ogilvie & Latter (2013a).⁶ Here we evaluate Q_2 and Q_3 at $\alpha = 0.019$ and $\epsilon = 0$, for simplicity. In general, one must solve the two vectorial components of Equation (38) simultaneously. But for the purposes of presenting simplified solution, we consider only the amplitude of that equation. For the $|U|$ in Panels (b) and (c) to be equal at all r , the disks must have warp profiles $|\psi|(r)$ as shown Panel (d). The steady-state inclination structure $\beta(r)$ can then be inferred, as we shown in Panel (e).

4.4. Stability and the Maximum Warp

Now we take a closer look at the relationship between the sloshing amplitude $|U|$ and the warp amplitude $|\psi|$, shown in Panel (c) of Figure 7. While the linear theory predicts $U \propto \psi$ indefinitely, the nonlinear results

based on Ogilvie & Latter (2013a) demonstrate that U saturates. For our choice of $\alpha = 0.019$ and $\epsilon = 0$, the sloshing reaches a maximum at a critical warp amplitude $|\psi|_{\text{crit}} \approx 0.3$. Beyond this point, the $|U|$ - $|\psi|$ relation enters a declining branch where further increases in warp amplitude actually diminish the driven sloshing motion.

This declining branch indicates a dynamical instability, as a steady-state warp is stably only if $\partial_{|\psi|} U > 0$. Physically, if a stable disk is slightly over-warped, it generates a stronger sloshing (i.e., a stronger internal torque) that acts to restore the equilibrium. On the declining branch, however, an increase in $|\psi|$ weakens the sloshing (i.e. weakens the restoring torque), leading to a runaway growth of the warp (also see Dogan et al. 2018). Consequently, no continuous steady-state solution can exist if the required warp amplitude exceeds $|\psi|_{\text{crit}}$.

This warp instability imposes a physical limit for disk misalignment. As we shown in Panels (e) and (d), increasing β_{out} causes the entire $|\psi|$ profile to increase. Panel (f) shows the maximum values of the steady-state $|U|$ and $|\psi|$ profiles as functions of β_{out} : when we increase β_{out} near a critical value, the peak of the warp profile quickly approaches $|\psi|_{\text{crit}}$ and the amplitude of

⁶ To obtain Q_2 and Q_3 , we first solve Equations (74)–(78) in Ogilvie & Latter (2013a), which are coupled time-dependent equations for the fluid velocities and densities, with parameters $|\psi|$, α , and ϵ , and find the periodic solution with a shooting method. We then insert this solution into their Equation (92), which provides their $Q_4|\psi| = (Q_2 + iQ_3)|\psi|$. That quantity is equivalent to our $Q_2\psi + Q_3\hat{\ell}\times\psi$, after accounting for the difference between the complex and vector representations.

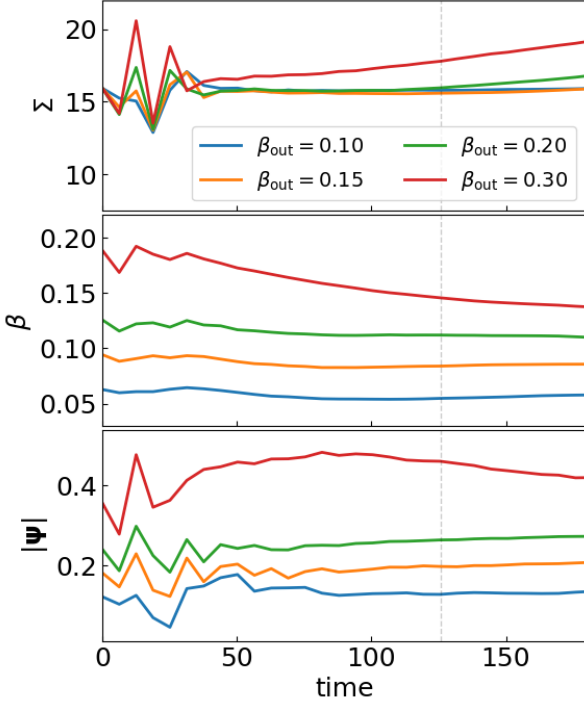


Figure 8. Time evolution of the disk density Σ , inclination β and warp amplitude $|\psi|$ at $r = 1.5$ in the simulations with β_{out} from 0.1 to 0.3 (C10 to C30 in Table 1). The vertical dashed lines mark $t = 125.6$, at which we analyze the simulation snapshots in later Figures.

$|\mathbf{U}|$ saturates; both indicate that the disk can no longer generate the required torque to maintain the warp. If β_{out} continues to increase, smooth steady-state warp profiles must then fail due to instability, leading to the so-called disk breaking.

5. NONLINEAR STEADY-STATE SIMULATIONS

We now examine the nonlinear regime using a suite of simulations, where the outer boundary inclination β_{out} is varied from 0.1 and 0.3 (models C10 to C30 in Table 1). To facilitate convergence, we initialize the disks using linear steady-state solutions for the inclination profile (β, γ) and sloshing velocity (u_r). While these initial conditions are not solutions to the nonlinear warp equations, they allow the tilting profiles to settle quickly into nonlinear steady states.

We let the disks evolve to reach their warp steady state. Figure 8 shows the time evolution of Σ , β , and $|\psi|$ at $r = 1.5$ for models C10 to C30: all three measurements have become quasi-steady in $t \sim 50$ after the initial transients fade. Subsequently, the density gap gradually fills, leaving the slow long-term warp evolution.

We focus on the snapshots from the simulations at $t = 125.6$, when the warps are sufficiently steady, in the

rest of this Section. Figure 9 shows side-views and the radial structures of these disks. As the outer inclination increases, the overall warp amplitude $|\psi|$ grows. Notably, except for the most extreme $\beta_{\text{out}} = 0.3$ case, the linear theory (shown as the faint curves in the right panels) are still provides a reasonable approximation for the β and ψ structure.

5.1. Internal Torque

We first verify the global torque profile. We Σ , \mathcal{L} and \mathbf{G} measured using Equations (15), (16) and (30), respectively; the in-plane torque is then calculated as

$$\mathbf{G}_{\perp} = \mathbf{G} - (\mathbf{G} \cdot \hat{\mathbf{l}}) \hat{\mathbf{l}} \quad (39)$$

for each snapshot. The top panel of Figure 10 shows the measured magnitude of \mathbf{G}_{\perp} as solid curves. Consistent with our nonlinear steady-state condition Equation (31), $|\mathbf{G}_{\perp}|^2$ is nearly constant across the warped region, except for the $\beta_{\text{out}} = 0.3$ case (red).

We pointed out in Section 4.1 that the approximation $\partial_r |\mathbf{G}_{\perp}| \simeq 0$ is accurate only if \dot{M} , $\partial_t \hat{\mathbf{l}}$, and viscous effects are all small; more specifically, we show in Appendix C.2 that the accuracy of Equation (31) can be quantified by the relation

$$\partial_r |\mathbf{G}_{\perp}|^2 \simeq -2\mathbf{G}_{\perp} \cdot \underbrace{\left(M r \Omega \psi + \Sigma \Omega r^2 \partial_t \hat{\mathbf{l}} \right)}_{\dot{\mathbf{L}}^* \text{ (error term)}}. \quad (40)$$

The first term in $\dot{\mathbf{L}}^*$ is due to the diversion of 3D accretion flow, while the second term accounts for the slow time evolution of $\hat{\mathbf{l}}$. The bottom panel of Figure 10 shows the excellent agreement between both sides of Equation (40) in all simulations. Indeed, we find that $|\mathbf{G}_{\perp}|^2 + \int \mathbf{G}_{\perp} \cdot \dot{\mathbf{L}}^* dr$ does not change with r as shown by the faint curves in the top panel. We also note that, for the $\beta_{\text{out}} = 0.3$ case, the M term is the primary contribution to the nonzero $\partial_r |\mathbf{G}_{\perp}|$, while the $\partial_t \hat{\mathbf{l}}$ term is subdominant. We shall discuss the origin of \dot{M} in Section 5.3.

Now we move on to verify the second nonlinear Equation (38). We measure the sloshing vector $\mathbf{U} = -\mathbf{G}_{\perp}/\sigma$ and plot the local $|\mathbf{U}|-|\psi|$ relation across various radii between 1.2 and 1.6 in Figure 11 as colored dots. The black line shows the prediction for based on the nonlinear shearing-box model in Ogilvie & Latter (2013a), while the faint gray line represents the linear relation based on our disk model. The measured results show an excellent agreement to the nonlinear theory. The sloshing amplitude saturates at $|\mathbf{U}| \approx 2$ with $|\psi| \sim 0.3$. At $|\psi| \gtrsim 0.3$, the amplitude of $|\mathbf{U}|$ is flat but appears starting to decrease with $|\psi|$, foreshadowing the instability if β_{out} becomes even higher.

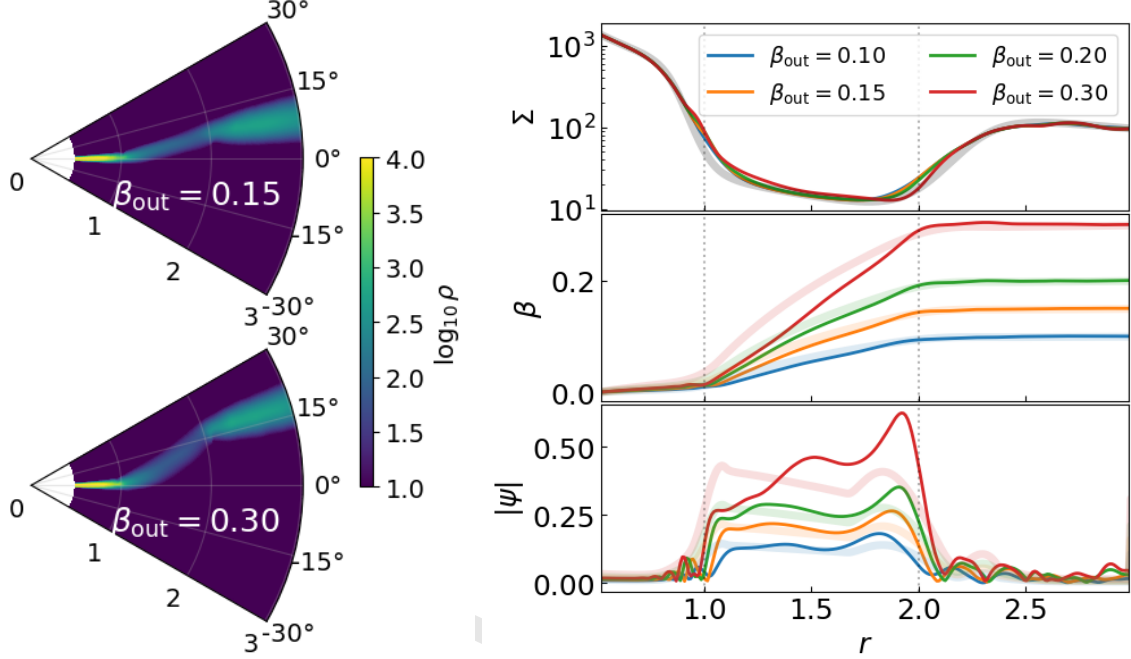


Figure 9. Snapshots of simulations with $\beta_{\text{out}} = 0.1$ to 0.3 at $t = 125.6$, which all show steady and continuous warps. **Left:** Two side views of the disk volume density ρ (at $\phi = 0$). **Right:** Surface density Σ , inclination profile β , and warp amplitude $|\psi|$ profiles. The solid lines are the measurements from simulations. The faint gray line in the top panel shows the initial density profiles, while the colored faint lines in the other two panels show the linear theory predictions.

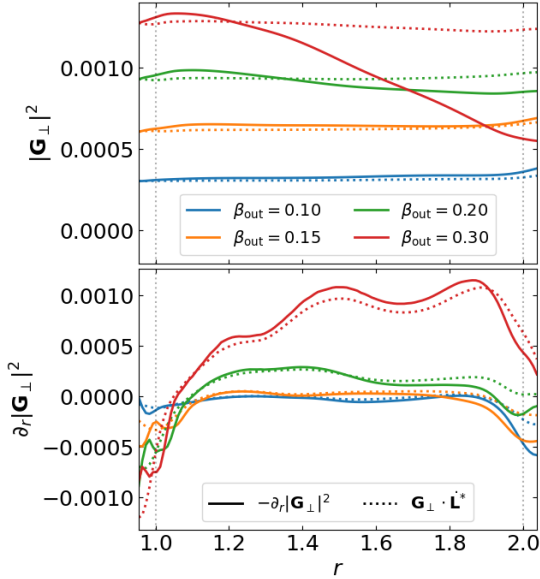


Figure 10. Diagnose of the internal torque from the nonlinear simulations. We measure \mathbf{G}_{\perp} and compute $\dot{\mathbf{L}}^*$ (defined in Equation 40). **Top:** Solid curves show the measurement of $|\mathbf{G}_{\perp}|^2$, while the dotted curves incorporate the error estimation by showing $|\mathbf{G}_{\perp}|^2 + \int \mathbf{G}_{\perp} \cdot \dot{\mathbf{L}}^* dr$. **Bottom:** Direct comparison between of $\partial_r |\mathbf{G}_{\perp}|^2$ and $\mathbf{G}_{\perp} \cdot \dot{\mathbf{L}}^*$.

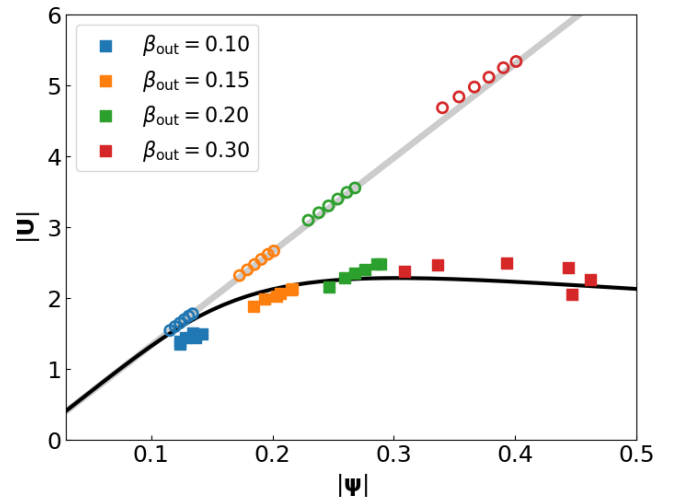


Figure 11. Relation between $|\mathbf{u}_r|$ and $|\psi|$ in simulations with different β_{out} (i.e., C10 to C30 in Table 1). The black line shows the prediction for $\alpha = 0.0189$ and $\epsilon = 0$ based on the shearing-box model in Ogilvie & Latter (2013a), while the faint gray line represents the linear relation. The scattered points show the values for $|\mathbf{u}_r|$ and $|\psi|$ measured from the simulations. Each color represents one simulation with a different β_{out} , while the dots with the same color correspond to the results measured at $r = 1.2, 1.3, \dots, 1.6$. The open circles and the solid squares shows the measurement at $t = 0$ and 125.8, respectively.

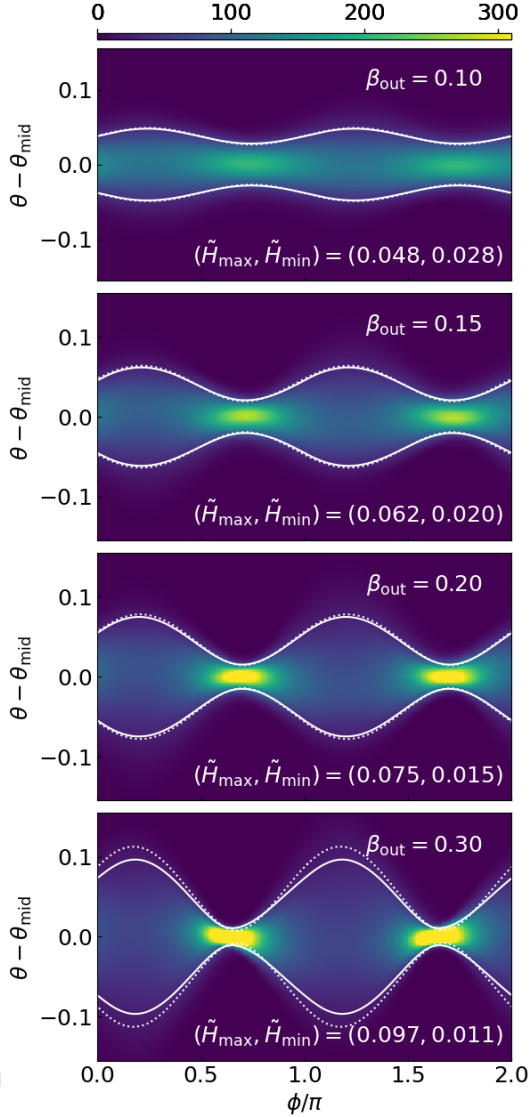


Figure 12. Simulated gas density distribution at $r = 1.5$ in four moderately warped disks at $t = 125.6$. The θ coordinates have been shifted to place the disk midplane at the center of the vertical axis. The solid white lines trace the disk scale height measured using Equation (41), while the dotted lines are the predictions based on Ogilvie & Latter (2013a).

Before moving to the breaking case, we wrap up the steady cases by further diagnosing the nonlinear effects that causes \dot{M} to saturate and \dot{M} .

5.2. Saturation and Bouncing

The saturation of the internal torque is rooted in the so-called ‘‘bouncing’’ effect, which is a nonlinear feature caused by the oscillating vertical pressure gradient experienced by the fluid elements in a warped disk. The top row of Figure 12 shows the vertical density distribution of the disks at $r = 1.5$ across the full azimuthal

range $\phi \in [0, 2\pi]$. As the warped amplitude grows, the disk develops a stronger ‘‘bouncing’’ feature, shown as the extreme vertical compression and expansion of the gas as it circulates along the $\hat{\phi}$ direction.

This bouncing feature leads to U saturating because it lowers density in regions where the sloshing motion v_r is large, as shown in the bottom row of Figure 12; while U can be considered as the mass-averaged sloshing amplitude, its growth is thereby limited when the warp gets strong. Physically, this can also be thought of as the saturation of Reynold stress, with the growth of \mathbf{v} being offset by the decrease in ρ .

We quantify the bouncing amplitude by measuring the local scale height \tilde{H} of the disk, defined as the standard deviation of the vertical density distribution:

$$\tilde{H}(r, \phi) = \left[\frac{1}{\Sigma} \int_0^\pi \rho (\theta_{\text{mid}} - \theta)^2 r^3 d\theta \right]^{1/2}, \quad (41)$$

where θ_{mid} is the polar angle of the disk midplane. In the most extreme case with $\beta_{\text{out}} = 0.3$, the local scale height \tilde{H} at $r = 1.5$ fluctuates between a minimum of 0.011 and a maximum of 0.097, which is a nearly ten-fold variation compared to the unperturbed value of $H = 0.037$.

We compare our simulation results for \tilde{H} to the local shearing-box theory of Ogilvie & Latter (2013a), calculated using their Equations (74) to (78) with $\alpha = 0.019$, $\epsilon \simeq 0$ and the simulated $|\psi|$ values. As shown by the dotted lines in the top row of Figure 12, the predictions match the simulation snapshots with remarkable accuracy.

5.3. Accretion Rate

In Section 5.1 we discussed the importance of \dot{M} . The simulation results for Σ and $\partial_r |\mathbf{G}_\perp|$ (as shown in Figures 9 and 10) both evolve differently depending on the warp amplitude. To quantify our result, we measure the mass accretion rate,

$$\dot{M}(r) = \int v_r \rho dS, \quad (42)$$

within density gap ($1 < r < 2$).

As shown in 13, the measured accretion rate is significantly enhanced in disks with stronger warps. This is also an effect caused by the internal stress of the disk. Based on the mass and angular momentum conservation, the nonlinear accretion is predicted to be

$$\dot{M} \partial_r \ell = -\partial_r (\mathbf{G} \cdot \hat{\mathbf{l}}) - \frac{1}{r} \sigma Q_2 |\psi|^2, \quad (43)$$

for which we reviewed the derivation in Appendix B.1, and is same as Equation (49) of Ogilvie (1999).

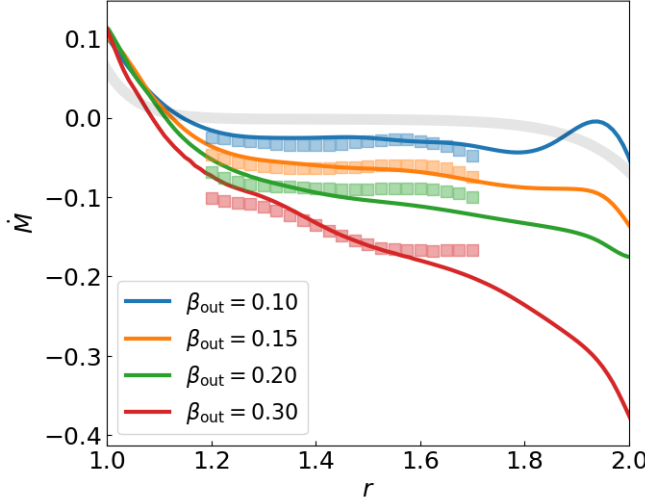


Figure 13. Mass flux \dot{M} at the $t = 125.6$. The colored curves show measurements from the simulations using Equation (42), from $r = 1$ to 2. The scattered boxes represent the predictions based on the Equation (43), where we calculated Q_1 using the shearing-box model in Ogilvie & Latter (2013a) with the real-time local values of $|\psi|$, $\alpha = 0.019$, and $\epsilon = 0$. The faint gray curve corresponds to the theoretical accretion rate if we assume the disk is flat.

To test Equation (43), we use Ogilvie & Latter (2013a)'s model to calculate the predicted values of $\mathbf{G} \cdot \hat{\ell}$ and Q_2 using the real-time local values of $|\psi|$; plugging them into Equation (43) along with simulated values for σ and ℓ yields a theoretical prediction for \dot{M} .⁷ We show this prediction in Figure 13 as scattered boxes and find good agreement with the \dot{M} values from direct measurement.

6. BROKEN DISK

Now we look at the simulation with $\beta_{\text{out}} = 0.4$, the broken disk. The left-hand-side panels of Figure ?? show snapshots of the density field from the simulation. The disk begins as a continuous warp ($t = 0$); as it evolves ($t \sim 62.8$ to ~ 125.6), the inner and outer disk regions gradually detach, forming two disconnected planes separated by a narrow density gap at $r \simeq 1.5R_0$. After falling apart, the two disk portions quickly flatten themselves ($t \sim 188.4$), with the inner and outer disks eventually aligned to $\beta_{\text{in}} = 0$ and $\beta_{\text{out}} = 0.4$, respectively.

The right-hand-side panels of Figure ?? illustrate the time evolution of the density, inclination, and warp amplitude profiles during the breaking process. The inclination profile β gradually steepens, eventually produc-

ing a sharp jump at the breaking point $r \simeq 1.5R_0$. The warp ψ initially spread nearly uniformly between $r = 1$ and $r = 2$; during the evolution, ψ becomes extremely localized, with the maximum $|\psi|$ increasing from ~ 0.5 at early times to as high as ~ 8 in the final snapshot. While the old density gap is filling up at $r \sim 1$ and ~ 2 , a new sharp density gap gradually depletes at the breaking radius, where Σ decreases by a factor of ten, suggesting that mass flux is significantly enhanced by the strong warp.

This breaking process is spontaneous: no explicit external forces are tearing the disk. The evolution of this disk agrees with the prediction in Section 4: a disk cannot maintain a steady warp when β_{out} is larger than a critical value. Our empirical limit of β_{out} for breaking is between 0.3 and 0.4, while the simplified model in Section 4 predicts breaking at $\beta_{\text{out}} \simeq 0.3$.

6.0.1. Unbreaking

To further confirm that $\beta_{\text{out}} \simeq 0.4$ is a robust condition for disk breaking, we perform three additional simulations with the following setups:

- We hold β_{out} of the simulated disks at 0.2, 0.3, 0.4.
- We set up the disk background Σ and Ω profiles to be the same in other simulations, but apply a step-function initial inclination profile

$$\beta(r) = \begin{cases} 0 & \text{if } r < 1.5, \\ \beta_{\text{out}} & \text{if } r > 1.5, \end{cases} \quad (44)$$

so that the disk are nearly broken from the beginning.

- We do not put in any initial sloshing motion (i.e., $\mathbf{u}_r = 0$), because the warp amplitude is zero everywhere (except at the $r = 1.5$).

These three simulations are referred to as C20unbreak, C30unbreak, and C40unbreak in Table 1.

Figure 14 shows the radial profiles of the disks measured from late-time simulation snapshots. The disks with $\beta_{\text{out}} = 0.2$ and 0.3 reattach their inner and outer parts, as shown by their continuous β and small $|\psi|$ in the final snapshots.

However, the disk with $\beta_{\text{out}} = 0.4$ remains broken: despite some small evolutions, the β profile remains approximately a step function, $|\psi|$ is nearly zero everywhere except at the breaking location, and the Σ profile gradually opens a narrow gap at where $|\psi|$ peaks.

These additional simulations show that, in our setup, the breaking and the continuity of the disk depend on β_{out} , rather than the initial $\beta(r)$ profile. When

⁷ The theoretical values for $\mathbf{G} \cdot \hat{\ell}$ is calculated as $\mathbf{G} \cdot \hat{\ell} = -\sigma Q_1$, where Q_1 is obtained using (91) from Ogilvie & Latter (2013a). We assume $\epsilon = 0$ when calculating Q_1 and Q_2 .

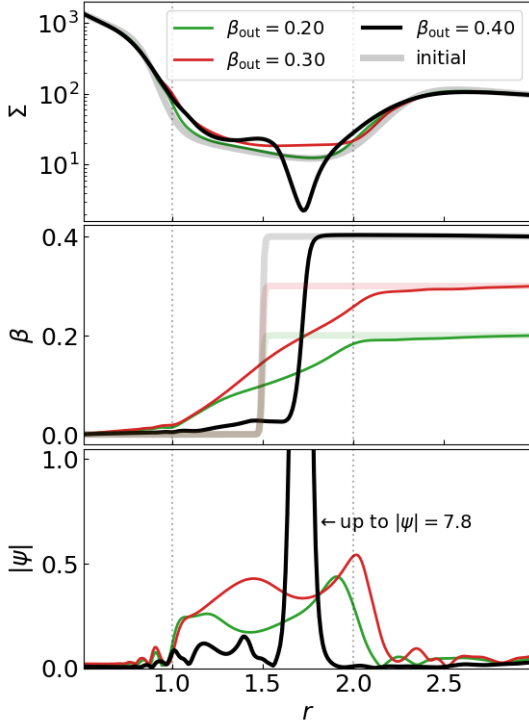


Figure 14. Surface density Σ , inclination profile β , and warp amplitude $|\psi|$ measured from three simulation snapshots: C20unbreak with $\beta_{\text{out}} = 0.2$ at $t = 113$, C30unbreak with $\beta_{\text{out}} = 0.3$ at $t = 232$, and C40unbreak with $\beta_{\text{out}} = 0.4$ at $t = 201$. The faint gray line in the top panel shows the initial density profile, while the colored faint lines in the middle panel show the initial inclination profiles.

$\beta_{\text{out}} \leq 0.3$, the disk will reach a WSS with continuous warp structures, even if it starts as two completely misaligned flat plates. When $\beta_{\text{out}} \gtrsim 0.4$, the steady state is a broken state, where the disk holds a step-function β profile with a sharp transition at the middle of the disk; the inner and outer parts of the disks flatten to β_{in} and β_{out} , respectively.

6.0.2. Discussion

As we have discussed in Section 4, the $|u_r|$ - $|\psi|$ curve determines the maximum β_{out} before disk breaking. The shearing-box model from Ogilvie & Latter (2013a) suggest that the critical β_{out} is slightly less than 0.3 (lower-right of Figure 7). However, our simulation with $\beta_{\text{out}} = 0.3$ does not break. The empirical β_{out} limit for breaking is between 0.3 and 0.4.

There are a few possible explanation to why this disk does not break. One example is that the breaking conditions is affected by shock. In a strongly warped (but not yet broken) disk, gas compresses and expands two times per orbit. These compression become supersonic at large amplitude and may produce shocks that damp

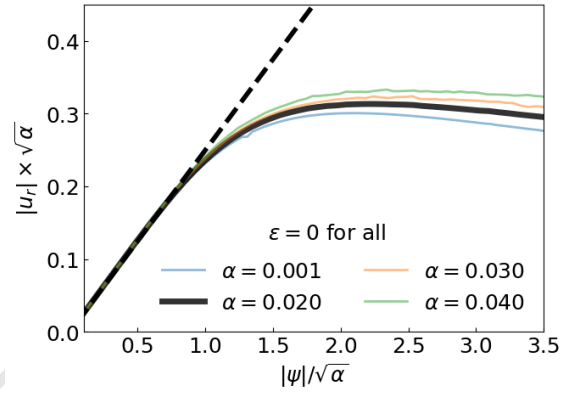


Figure 15. Steady-state relation between sloshing u_r and warp amplitude $|\psi|$. The solid curves show the prediction from the shearing-box model of Ogilvie & Latter (2013a) for $\epsilon = 0$ and different viscosity α , while the dashed line shows the linear prediction for $\alpha = 0.02$ and $\epsilon = 0$.

the warp (Held & Ogilvie 2024; Kaaz et al. 2025), suppressing the breaking process. Figure 11 shows that the steady state of this disk has $\partial_\psi |u_r|$ marginally less than zero, so it is possible that the instability is not enough to overcome strong dissipation. However, we do not find clear evidence of shocking in our C30 simulation; recent work by Held & Ogilvie (2025) argues that shock may also facilitate disk breaking through density gap opening. Hence, we argue that the shock dissipation is irrelevant to the C30 case.

Another possibility is the numerical resolution. However, we have performed two suites of simulations with halved and doubled amounts of grid cells in θ -direction and found no qualitative difference in the outcomes. Nevertheless, it may be worth noting that the right-hand panels of Figure ?? show a slow outward drafting of the breaking radius. The rate of this outward drift appears faster in low-resolution runs. A follow-up study may be needed to investigate the long-term effects of this drifting.

We adopt $\alpha = 0.019$ in all simulations. To generalize the breaking condition to different α values, we the u_r - ψ relation using the shearing-box model (Ogilvie & Latter 2013a) and show the results in Figure 15. The $|u_r|$ - $|\psi|$ relation roughly scales with $\sqrt{\alpha}$. The curve become nonlinear when $|\psi| \gtrsim \sqrt{\alpha}$, while $|\psi|_{\text{crit}} \simeq 2\sqrt{\alpha}$. The maximum sloshing amplitude is roughly $|u_r| = 0.3\sqrt{\alpha}$.

7. CONCLUSION

In this work, we have carried out a systematic investigation of warp steady states (WSS) in accretion disks, spanning the linear, nonlinear, and breaking regimes. Our study combines linear analytic theory, local nonlinear models, and global three-dimensional hydrodynamic

simulations. Rather than including an explicit perturber or external torque, we fix the disk inclination angles β_{in} and β_{out} at the inner and outer boundaries. This setup provides a clean framework for diagnosing how the hydrodynamics of how disks bend, sustain coherent warps, and eventually break, while remaining agnostic about the origin of the warp.

For weakly warped disks, our simulations with $\beta_{\text{out}} = 0.033$ confirm the linear theory (Sections 2 and 3). We see disks rapidly relaxing to their respective WSS; their simulated warping and inclination profiles, sloshing velocity fields and internal torque fluxes show excellent agreement with the theoretic predictions. Importantly, the predictions remain accurate for real-time steady-state warp profiles even as the background density slowly evolves, implying that protoplanetary disks should stay in WSS on timescales much shorter than their viscous evolution.

As we increase β_{out} to inject stronger warps, disks enter the nonlinear regime where several new features emerge (Section ??). First, the internal torque no longer grows linearly with $|\psi|$, but instead it saturates. Second, the gas exhibits strong “bouncing” motions, undergoing cycles of vertical compression and expansion twice per orbital period; this effect leads to large azimuthal fluctuations in the local disk scale height. Third, large warp $|\psi|$ also enhance the mass accretion flows. All three effects are clearly measured in our simulations and are in good quantitative agreement with the nonlinear predictions (Ogilvie 1999; Ogilvie & Latter 2013a).

When the warp amplitude is increased further, nonlinear disks become unstable and may break (Section 6). We show in our $\beta_{\text{out}} = 0.4$ simulation that a strongly warped disk may undergo a runaway instability: the warp amplitude $|\psi|$ rapidly grows and localizes, and the disk eventually break into two misaligned pieces separated by a density gap. This breaking process occurs spontaneously from internal hydrodynamics, without requiring explicit external forcing. Our analysis verifies

that this instability happens when the large warp causes the torque to fully saturate so that $\partial_\psi(u_r) < 0$; under this condition, local increases in $|\psi|$ reduce the restoring torque, rather than enhancing it. The critical warp amplitude for instability is given by $|\psi|_{\text{crit}} \simeq 2\sqrt{\alpha}$ for Keplerian disks.

Overall, our work present a comprehensive picture of the hydrodynamics of warped disks, illustrating how disks may bend, sustain coherent warps, or break. We summarize the theoretical interpretation in Section 4.

Future work may explore the long-term behavior of broken disks. Some previous simulations have shown examples where disks can heal from breaking and reconnect into whole pieces (e.g., Deng & Ogilvie 2022), but the exact mechanism is not fully understood. Another extension is to incorporate additional physics, such as magnetic fields, turbulence, and gas self-gravity. Explicit perturbers may also be added to further connect our results to more specific astrophysical scenarios. One may also model the observational signatures of the nonlinear behaviors, such as bouncing and enhanced accretion, which may used for future detections of disk warping.

ACKNOWLEDGMENTS

We thank Nicholas Kaaz, Rixin Li, Alexander Dittmann, Diego Munoz, and Jeremy Rath for their stimulating discussion. Jiaru Li is supported by a CIERA Postdoctoral Fellowship. This work used computing resources provided by Northwestern University and the Center for Interdisciplinary Exploration and Research in Astrophysics (CIERA). This research was supported in part through the computational resources and staff contributions provided for the Quest high performance computing facility at Northwestern University which is jointly supported by the Office of the Provost, the Office for Research, and Northwestern University Information Technology.

APPENDIX

A. DERIVATION OF THE LINEAR THEORY

Here we derive the linearized equations of motion for a warp in a globally isothermal protoplanetary disk. The disk is governed by the momentum and continuity equations,

$$(\partial_t + \mathbf{v}_{\text{tot}} \cdot \nabla) \mathbf{v}_{\text{tot}} = -\nabla\Phi - c_s^2 \nabla \lambda_{\text{tot}}, \quad (\text{A1})$$

$$(\partial_t + \mathbf{v}_{\text{tot}} \cdot \nabla) \lambda_{\text{tot}} = -\nabla \cdot \mathbf{v}_{\text{tot}}, \quad (\text{A2})$$

where the subscript “tot” denotes the total value (background + perturbation), \mathbf{v}_{tot} is the velocity vector,

$$\lambda_{\text{tot}} = \ln \rho_{\text{tot}} \quad (\text{A3})$$

is the logarithm of the density, c_s is the globally constant sound speed, and Φ is the gravitational potential of the central star. We temporarily ignore viscosity.

We shall decompose

$$\lambda_{\text{tot}} = \lambda + \lambda' \quad (\text{A4})$$

$$\mathbf{v}_{\text{tot}} = \mathbf{v} + \mathbf{v}' \quad (\text{A5})$$

where unsubscripted λ and \mathbf{v} denote the background, and primed quantities denote the perturbation.

A.1. Background

The background is taken to be axisymmetric and aligned with the vertical axis. In cylindrical coordinates (R, ϕ, z) , $\mathbf{v} = (v_R, v_\phi, v_z) = (0, R\Omega, 0)$. The angular frequency $\Omega(R, z)$ and $\lambda(R, z)$ are related by

$$R\Omega^2 = c_s^2 \partial_R \lambda + \partial_R \Phi, \quad (\text{A6})$$

$$0 = c_s^2 \partial_z \lambda + \partial_z \Phi \quad (\text{A7})$$

based on Equation (A1).

Taking $\partial_z(\text{A6}) - \partial_R(\text{A7})$ gives $\partial_z \Omega = 0$. Hence, Ω can be determined by evaluating Equation (A6) at the midplane, which yields

$$\Omega^2 = \Omega_K^2 + \frac{c_s^2}{R} \partial_R \lambda_{\text{mid}} \quad (\text{A8})$$

where $\Omega_K = \Omega_K(R)$ is the Keplerian frequency and $\lambda_{\text{mid}} = \lambda|_{z=0}$.

Taking $z \times (\text{A6}) - R \times (\text{A7})$ leads to

$$\partial_z \lambda = -\frac{z}{H^2} + \frac{z}{R} \partial_R \lambda, \quad (\text{A9})$$

where

$$H = c_s / \Omega. \quad (\text{A10})$$

Near the midplane of the disk, the first term on the right-hand side is dominant over the second as $H^2 \ll R^2$, so $\rho \propto \exp\{-z^2/(2H^2)\}$. Therefore, the background volume density of the disk has the form

$$\rho(R, z) = \frac{\Sigma}{\sqrt{2\pi} H} \exp\left\{-\frac{z^2}{2H^2}\right\}, \quad (\text{A11})$$

where $\Sigma(R)$ is the radial profile of the disk surface density, which can be chosen freely.

In terms of Σ , Equation (A8) becomes

$$\Omega^2 = \Omega_K^2 + \frac{c_s^2}{R} \partial_R \ln\left(\frac{\Sigma}{H}\right). \quad (\text{A12})$$

We shall also need the epicyclic frequency,

$$\kappa^2 \equiv R^{-3} \partial_R (R^4 \Omega^2) \quad (\text{A13})$$

and its deviation from Ω via

$$\epsilon \equiv \frac{\kappa^2}{\Omega^2} - 1 \quad (\text{A14})$$

$$= R \partial_R \ln(\Omega^2 R^3) \quad (\text{A15})$$

$$\approx R \partial_R \left(\frac{H^2}{R^2} R \partial_R \ln \frac{\Sigma}{H} \right) \quad (\text{A16})$$

where the final expression is to leading order in H^2/R^2 when $d_R(\ln \Sigma)$ is order unity.

A.2. Perturbation Equations

Linearizing Equations (A1) and (A2) yields

$$\partial_t v'_R = -\Omega \partial_\phi v'_R + 2\Omega v'_\phi - c_s^2 \partial_R \lambda', \quad (\text{A17})$$

$$\partial_t v'_\phi = -\Omega \partial_\phi v'_\phi - (2 + R \partial_R \ln \Omega) \Omega v'_R - \frac{c_s^2}{R} \partial_\phi \lambda', \quad (\text{A18})$$

$$\partial_t v'_z = -\Omega \partial_\phi v'_z - c_s^2 \partial_z \lambda', \quad (\text{A19})$$

$$\partial_t \lambda' = -\Omega \partial_\phi \lambda' - \frac{1}{R} \partial_R (R v'_R) - (\partial_R \lambda) v'_R - \frac{1}{R} \partial_\phi v'_\phi - (\partial_z \lambda) v'_z - \partial_z v'_z, \quad (\text{A20})$$

Following Tanaka et al. (2002) and Ogilvie (2008), we take the azimuthal dependency of linearized variables to be $\propto e^{-i\phi}$, as is appropriate for a warp, and we decompose the vertical dependency in Hermite polynomials. We further simplify by restricting the Hermite expansion to the leading-order contributions, which results in setting

$$\frac{v'_R}{\Omega R} = U_R \frac{z}{H} e^{-i\phi}, \quad (\text{A21})$$

$$\frac{v'_\phi}{\Omega R} = U_\phi \frac{z}{H} e^{-i\phi}, \quad (\text{A22})$$

$$\frac{v'_z}{\Omega R} = U_z e^{-i\phi}, \quad (\text{A23})$$

$$\lambda' = \Lambda \frac{z}{H} e^{-i\phi}, \quad (\text{A24})$$

where U_R , U_ϕ , U_z , and Λ are complex coefficients that depend on R and t . Plugging these into Equations (A17) to (A20) gives the evolution equations

$$\Omega^{-1} \partial_t U_R = iU_R + 2U_\phi + h^2 R(\partial_R \ln H)\Lambda - h^2 R \partial_R \Lambda, \quad (\text{A25})$$

$$\Omega^{-1} \partial_t U_\phi = iU_\phi - (2 + R \partial_R \ln \Omega) U_R + ih^2 \Lambda, \quad (\text{A26})$$

$$\Omega^{-1} \partial_t U_z = iU_z - h\Lambda, \quad (\text{A27})$$

$$\Omega^{-1} \partial_t \Lambda = i\Lambda - R \partial_R \ln (\Omega \Sigma H R^2) U_R - R \partial_R U_R + iU_\phi + \frac{1}{h} U_z - h R \partial_R \ln (\Sigma H^2) U_z, \quad (\text{A28})$$

where

$$h = H/R \quad (\text{A29})$$

is the aspect ratio. To derive Equation (A28), we use Equations (A9) and (A11) to calculate $\partial_z \lambda$ and $\partial_R \lambda$, respectively. In addition, although the factors of z cancel from the first three equations, some of the terms in Equation (A28) have coefficient z , and others have coefficient z^3 . Since we are really extracting the projection of this equation onto the first Hermite polynomial, we replace those coefficients by their projections, which amounts to replacing $z \rightarrow H$ and $z^3 \rightarrow 3H^3$.

A.3. Steady-State Equations

Henceforth, we consider steady-state equations ($\partial_t \rightarrow 0$). Equation (A27) gives $\Lambda = iU_z/h$, which can be used to eliminate Λ in other three equations. We then eliminate U_ϕ by forming two different combinations of the three equations: $-i \times (\text{A25}) + 2 \times (\text{A26})$ and $-i \times (\text{A25}) + (\text{A26}) + (\text{A28})$. These combinations gives

$$0 = \frac{d}{dR} [\Sigma H \Omega^2 R^3 (U_R + hU_z)], \quad (\text{A30})$$

$$0 = \frac{d \ln (\Omega^2 R^3)}{dR} (U_R + hU_z) + h \frac{d}{dR} U_z, \quad (\text{A31})$$

which are two equations for two unknowns: $U_R + hU_z$ and U_z . The former is related to the radial speed in the (spherical) $\hat{\mathbf{r}}$ direction, $v'_r = (R/r)v'_R + (z/r)v'_z$, which implies

$$\frac{v'_r}{\Omega R} \approx (U_R + hU_z) \frac{z}{H} e^{-i\phi} \quad (\text{A32})$$

after dropping the $O(z^2/r^2)$ correction. We therefore define

$$U_r \equiv U_R + hU_z \quad (\text{A33})$$

which represents the amplitude of v'_r . Equations (A30–A31) then become

$$0 = \frac{d}{dR} (\Sigma H \Omega^2 R^3 U_r), \quad (\text{A34})$$

$$0 = \epsilon U_r + hR \frac{d}{dR} U_z. \quad (\text{A35})$$

We will show in A.4 that viscosity contributes an extra $-2i\alpha U_r$ term to the right-hand-side of Equation (A35).

Equations (2) and (3) then follow after defining

$$W \equiv -iU_z, \quad u_r = \frac{R}{H} U_r \quad (\text{A36})$$

and adding the viscous term.

A.4. Viscous Terms

Here, we derive the viscous term we added in the last step of the previous section. We take the viscous force per unit mass to be

$$\mathbf{f}_{\text{tot}} = \frac{1}{R\Omega^2 \rho_{\text{tot}}} \nabla \cdot (\nu \rho_{\text{tot}} \boldsymbol{\tau}_{\text{tot}}), \quad (\text{A37})$$

where $\boldsymbol{\tau}$ is the stress tensor and ν is the kinematic viscosity,

$$\nu = \alpha c_s H, \quad (\text{A38})$$

with α being the viscosity parameter as in the Shakura & Sunyaev (1973) model. This \mathbf{f}_{tot} is to be added to the right-hand side of Equation (A1).

We derive the perturbed \mathbf{f}' , which is to be inserted on the right-hand-side of the steady-state versions of Equations (A17)–(A19) by first working in the zero-inclination frame, where $v'_z = 0$. We shall then rotate to obtain the general form. Anticipating that the vertical viscous force is small, Equation (A19) implies $\lambda' = 0$. Then,

$$\mathbf{f}' = \frac{1}{R\Omega^2 \rho} \nabla \cdot (\nu \rho \boldsymbol{\tau}'). \quad (\text{A39})$$

The most important terms in $\boldsymbol{\tau}'$ are

$$\tau'_{Rz} = \tau'_{zR} = \partial_z v'_R, \quad (\text{A40})$$

$$\tau'_{\phi z} = \tau'_{z\phi} = \partial_z v'_\phi, \quad (\text{A41})$$

as the main effect of viscosity is to act on the sloshing-induced vertical shear in the horizontal velocity components (see also Papaloizou & Lin 1995). Hence,

$$\mathbf{f}' \simeq \frac{1}{R\Omega^2 \rho} \frac{\partial}{\partial z} \left[\nu \rho \left(\hat{\mathbf{R}} \partial_z v'_R + \hat{\phi} \partial_z v'_\phi \right) \right] \quad (\text{A42})$$

$$\simeq -\frac{\alpha z}{R\Omega} \left[(\partial_z v'_R) \hat{\mathbf{R}} + (\partial_z v'_\phi) \hat{\phi} \right] \quad (\text{A43})$$

$$\simeq -\frac{\alpha v'_R}{R\Omega} \left[\hat{\mathbf{R}} + \left(\frac{i}{2} \right) \hat{\phi} \right], \quad (\text{A44})$$

where we keep leading order terms by assuming $\partial_R, \partial_\phi \rightarrow \mathcal{O}(1)$ and $\partial_z \rightarrow \mathcal{O}(1/h)$ (see also Papaloizou & Lin 1995), and in the third equality we eliminate v'_ϕ by using the dominant contribution from Equation (A17).

In order to rotate \mathbf{f}' , we simply replace $v'_R \rightarrow v'_r$; other contributions to the rotation are higher order. The result is that Equations (A25)–(A26) are to be modified by adding to their respective right-hand-sides $-\alpha U_r$ and $\frac{1}{2}i\alpha U_r$. Finally, when we carry through the manipulations described in Section A.3, the viscous force adds $-2i\alpha U_r$ to the right-hand side of Equation (A35). It also adds a term to Equation (A34), but one that is smaller than the other in Equation (A34) term by $\mathcal{O}(\alpha)$, and so we drop it. Our viscous term is the same as those in Papaloizou & Lin (1995) and Lubow & Ogilvie (2000), except that their terms are proportional to U_R .

B. NONLINEAR THEORY

To derive the equations governing a nonlinear warped disk, we follow the framework of Ogilvie & Latter (2013a). The global evolution is determined by the conservation of mass and angular momentum for a spherical shell:

$$\partial_t \mathcal{M} + \partial_r \mathcal{F} = 0, \quad (\text{B45})$$

$$\partial_t (\mathcal{M} \mathbf{h}) + \partial_r \mathbf{F}_L = 0, \quad (\text{B46})$$

Here \mathcal{M} is the mass per unit radius and \mathbf{h} is the specific angular momentum, defined as

$$\mathcal{M} = \int \rho dS, \quad (\text{B47})$$

$$\mathbf{h} = \frac{1}{\mathcal{M}} \int \rho (\mathbf{r} \times \mathbf{v}) dS \quad (\text{B48})$$

with $dS \equiv r^2 \sin \theta d\theta d\phi$. The terms \mathcal{F} and \mathbf{F}_L are the radial flux of mass and angular momentum,

$$\mathcal{F} = \int v_r \rho dS, \quad (\text{B49})$$

$$\mathbf{F}_L = \int v_r \rho (\mathbf{r} \times \mathbf{v}) dS + \mathbf{F}_\nu, \quad (\text{B50})$$

with \mathbf{F}_ν being the viscous contribution.

We define the disk's orientation by the unit vector $\hat{\mathbf{l}} = \ell/\ell$, where $\ell = |\ell|$ is the magnitude of ℓ ; we assume the magnitude $\ell = r^2\Omega$ is fixed in time. To isolate the dynamics of the warp, we focus on the internal torque \mathbf{G} , defined as

$$\mathbf{G} \equiv \mathbf{F}_L - \mathcal{F} \mathbf{h}, \quad (\text{B51})$$

where we subtract the advective part from the total angular momentum flux. Substituting this into Equation (B46) and using Equation (B45), we obtain the equation for the tilt evolution:

$$\mathcal{M} h \partial_t \hat{\mathbf{l}} + \mathcal{F} \partial_r \mathbf{h} + \partial_r \mathbf{G} = 0. \quad (\text{B52})$$

Physically, Equation (B52) states that the disk's orientation changes due to the gradient of internal torques and the advection of angular momentum by the mass flow \dot{M} . In the interests of constraining \mathbf{G} , we write

$$\partial_r \mathbf{G} = - \left(\mathcal{M} h \partial_t \hat{\mathbf{l}} + \mathcal{F} \partial_r \mathbf{h} \right) = - \left[\mathcal{M} h \partial_t \hat{\mathbf{l}} + \frac{\mathcal{F} h}{r} \psi + (\mathcal{F} \partial_r h) \hat{\mathbf{l}} \right], \quad (\text{B53})$$

based on Equation (B52).

B.1. Accretion Flow \mathcal{F}

Following Ogilvie & Latter (2013a), we express the internal torque in terms of dimensionless coefficients Q 's:

$$\mathbf{G} = -\sigma \left(Q_1 \hat{\mathbf{l}} + Q_2 \psi + Q_3 \hat{\mathbf{l}} \times \psi \right), \quad (\text{B54})$$

for which we may consider as the sum of the parallel component, $\mathbf{G}_{\parallel} = -\sigma Q_1 \hat{\mathbf{l}}$, and the perpendicular component, $\mathbf{G}_{\perp} = -\sigma(Q_2 \psi + Q_3 \hat{\mathbf{l}} \times \psi)$. By projecting Equation (B52) onto $\hat{\mathbf{l}}$ direction, we find

$$\mathcal{F} \partial_r h + \hat{\mathbf{l}} \cdot \partial_r \mathbf{G} = 0, \quad (\text{B55})$$

where we can further note that $\hat{\mathbf{l}} \cdot \partial_r \mathbf{G} = \partial_r (\hat{\mathbf{l}} \cdot \mathbf{G}) - \mathbf{G} \cdot \partial_r \hat{\mathbf{l}}$ and get

$$\mathcal{F} \partial_r h = \partial_r (\sigma Q_1) - \frac{1}{r} \sigma Q_2 |\psi|^2, \quad (\text{B56})$$

which is the same as Equation (49) of Ogilvie (1999).

In the limit of small $|\psi|^2$, the last equation becomes $\mathcal{F} \partial_r h = \partial_r (\sigma Q_1)$, or simply

$$\mathcal{F} = \frac{\sigma Q_1}{h}, \quad (\text{B57})$$

for globally isothermal disk; if $|\psi|^2$ is large, the accretion flow \mathcal{F} is mainly driven by $Q_2 |\psi|^2$ and the Q_1 terms is negligible.

B.2. In-plane Torque \mathbf{G}_\perp

We now focus on the perpendicular component of the internal torque, $\mathbf{G}_\perp = -\sigma(Q_2\psi + Q_3\hat{\mathbf{l}} \times \psi)$, as it is fully caused by the warp. We find the radial derivative of its magnitude is given by

$$\partial_r |\mathbf{G}_\perp|^2 = 2\mathbf{G}_\perp \cdot \partial_r \mathbf{G}_\perp = 2\mathbf{G}_\perp \cdot (\partial_r \mathbf{G} - \partial_r \mathbf{G}_\parallel) = 2\mathbf{G}_\perp \cdot \left(\partial_r \mathbf{G} + \frac{\sigma Q_1}{r} \psi \right), \quad (\text{B58})$$

where, in the last step, we plug in $\partial_r \mathbf{G}_\parallel = -\partial_r(\sigma Q_1)\hat{\mathbf{l}} - \sigma Q_1 \partial_r \hat{\mathbf{l}}$ and dropped the $\hat{\mathbf{l}}$ term because it will dot to zero. Inserting Equation (B53) into the right-hand side of Equation (B58), we get

$$\partial_r |\mathbf{G}_\perp|^2 = 2\mathbf{G}_\perp \cdot \left(-\mathcal{M}h \partial_t \hat{\mathbf{l}} - \frac{\mathcal{F}h}{r} \psi + \frac{\sigma Q_1}{r} \psi \right), \quad (\text{B59})$$

where the terms in the parentheses represent the sources of torque variation.

Based on our \mathcal{F} discussion above, we have

$$\partial_r |\mathbf{G}_\perp|^2 = -2\mathcal{M}h \left(\mathbf{G}_\perp \cdot \partial_t \hat{\mathbf{l}} \right) \quad (\text{B60})$$

if $|\psi|^2$ is small. In the limit of large $|\psi|^2$,

$$\partial_r |\mathbf{G}_\perp|^2 = 2\mathbf{G}_\perp \cdot \left(-\mathcal{M}h \partial_t \hat{\mathbf{l}} - \frac{\mathcal{F}h}{r} \psi \right), \quad (\text{B61})$$

because the $\mathcal{F}h$ term dominates over the σQ_1 term.

B.3. Stability Analysis

Now we analyze the stability of the nonlinear solutions. Consider a state that is perturbed from an equilibrium by a small amount, i.e.,

$$\psi \rightarrow \psi_0 + \delta\psi, \quad (\text{B62})$$

For simplicity, we assume $\delta\psi$ and ψ_0 are in the same direction and let $\delta\psi \equiv |\delta\psi| \propto e^{\gamma t + ikr}$. We note that

$$\partial_{|\psi|} \mathbf{G} = -\sigma(\partial_{|\psi|} Q_1 \hat{\mathbf{l}} + \partial_{|\psi|} \mathbf{U}), \quad (\text{B63})$$

so we have

$$\delta\mathbf{G} = -\sigma(\partial_{|\psi|} Q_1 \hat{\mathbf{l}} + \partial_{|\psi|} \mathbf{U}) \delta\psi \quad (\text{B64})$$

for the torque perturbation.

The angular momentum equation gives

$$\frac{\mathcal{M}\ell}{r} \partial_t \psi + \mathcal{F} \partial_r^2 \ell + \partial_r^2 \mathbf{G} = 0, \quad (\text{B65})$$

where we have taken $\mathcal{M}\ell$ and \mathcal{F} to be constant of r by assuming steady-state isothermal disk. Subtracting the equilibrium from this equation, we get

$$\frac{\mathcal{M}\ell}{r} \partial_t \delta\psi + \mathcal{F} \partial_r \left(\frac{\delta\psi}{r} \right) + \partial_r^2 (\delta\mathbf{G}) = 0. \quad (\text{B66})$$

In the limit of large k , this equation simplifies to

$$\frac{\mathcal{M}\ell}{r} \gamma + \frac{ik\mathcal{F}}{r} + k^2 \sigma \partial_{|\psi|} |\mathbf{U}| = 0, \quad (\text{B67})$$

where we keep only terms in the direction of $\delta\psi$ and cancel out the common $\delta\psi$ factor. This suggest that

$$\gamma = -\frac{ik\mathcal{F}}{\mathcal{M}\ell} - \frac{k^2 \sigma r}{\mathcal{M}\ell} \partial_{|\psi|} |\mathbf{U}|, \quad (\text{B68})$$

hence, the growth rate of the perturbation, $\text{Re}(\gamma)$, has the opposite sign of $\partial_{|\psi|} |\mathbf{U}|$. Therefore the disk is unstable when $\partial_{|\psi|} |\mathbf{U}| < 0$.

C. MEASUREMENT OF DISK STATES IN SIMULATIONS

The linear and nonlinear theory in the main text adopts a set of variables, for which we define how we measure them from the simulations. We measure the surface density Σ as

$$\Sigma = \frac{1}{2\pi r} \int \rho ds, \quad (\text{C69})$$

where $ds = r^2 \sin \theta d\theta d\phi$. To connect it more directly to conservation law, we also measure the local shell mass (i.e. mass per radius r)

$$\mathcal{M} = \int \rho ds = 2\pi r \Sigma, \quad (\text{C70})$$

and the local shell angular momentum (i.e. angular momentum per radius r),

$$\mathbf{L} = \int \rho (\mathbf{r} \times \mathbf{v}) ds. \quad (\text{C71})$$

Note that \mathcal{M} and \mathbf{L} have the dimension of mass and angular momentum per radius. We then define the local tilt as
We then de

while the simulations are performed in real-valued space using 3D spherical frame. This Appendix shows how to related complex linear quantities and the simulation measurement.

C.1. Tilt Vector $\hat{\mathbf{l}}$ and Complex W

The tilt vector is defined as $\hat{\mathbf{l}} = \mathbf{L}/|\mathbf{L}|$, where \mathbf{L} is the total orbital angular momentum vector. We measure \mathbf{L} from our simulation as

$$\mathbf{L}(r) = r^2 \int_0^{2\pi} \int_0^\pi \rho_{\text{tot}} \mathbf{r} \times \mathbf{v}_{\text{tot}} \sin \theta d\theta d\phi \quad (\text{C72})$$

$$\simeq r \int_0^{2\pi} \int_{-\infty}^{+\infty} (\rho + \rho') (R \hat{\mathbf{R}} + z \hat{\mathbf{z}}) \times (v'_R \hat{\mathbf{R}} + \Omega R \hat{\phi} + v'_\phi \hat{\phi} + v'_z \hat{\mathbf{z}}) dz d\phi \quad (\text{C73})$$

where we have expanded the total fluid quantities into the background and the perturbation as in Equation (A4) in the second line. We also switch to the cylindrical coordinates as used in Section 2, which introduces a $\mathcal{O}(\beta^2)$ correction factor that we ignore.

In the *linear* model, we have

$$\mathbf{L}(r) \simeq \Omega R^3 \int_0^{2\pi} \int_{-\infty}^{+\infty} \left[\hat{\mathbf{z}} - \frac{v'_z}{\Omega R} \hat{\phi} + \frac{z}{R} \frac{v'_R}{\Omega R} \hat{\phi} - \frac{z}{R} \frac{v'_\phi}{\Omega R} \hat{\mathbf{R}} - \lambda' \frac{z}{R} \hat{\mathbf{R}} \right] \rho dz d\phi, \quad (\text{C74})$$

where we have set $r = R$, dropped the nonlinear terms, dropped terms that are antisymmetric in z based on Equations (A21) to (A24).

Inserting the real parts of Equations (A21) to (A24) into the equation above, we can perform the integration and get

$$\mathbf{L} = 2\pi \Sigma \Omega R^3 [\text{Re}(V), \text{Im}(V), 1], \quad (\text{C75})$$

where

$$V = \frac{1}{2} (-iU_z + ihU_R - hU_\phi - h\Lambda). \quad (\text{C76})$$

In a steady state,

$$V = W + \mathcal{O}(hU_r + hU_\phi), \quad (\text{C77})$$

where we have used $\Lambda = iU_z/h$ and $W = -iU_z$, and we infer that

$$\mathcal{O}(hU_R) = \mathcal{O}(hU_\phi) = \mathcal{O}(hU_r) = \mathcal{O}\left(\frac{h^2}{2\alpha + i\epsilon} \psi\right) \ll |U_z| \quad (\text{C78})$$

when ψ is small and $h \lesssim |2\alpha + i\epsilon|$ (i.e., when non-resonant). Hence, we get

$$\hat{\mathbf{l}} \equiv \frac{\mathbf{L}}{|\mathbf{L}|} \simeq [\text{Re}(W), \text{Im}(W), 1], \quad (\text{C79})$$

which is introduced in Section 2 of the main text. It follows that

$$\psi = \frac{d\hat{\mathbf{l}}}{d \ln r} = [\text{Re}(\psi), \text{Im}(\psi), 1] \quad (\text{C80})$$

Hence, the complex numbers W and ψ are

$$W \simeq \hat{\mathbf{l}}_x + i\hat{\mathbf{l}}_y, \quad (\text{C81})$$

$$\psi \simeq \psi_x + i\psi_y, \quad (\text{C82})$$

where x and y subscripts are the Cartesian components of those vectors, as shown in Section 3.

C.2. Torque \mathbf{G} and Sloshing U_r

We measure the internal torque \mathbf{G} as

$$\mathbf{G}(r) = \frac{r^2}{2\pi} \int_0^{2\pi} \int_0^\pi (\mathbf{r} \times \mathbf{v}) v_r \rho d\theta d\phi. \quad (\text{C83})$$

from the simulations. Similar to what we do for \mathbf{L} , we have the *linear* approximation for \mathbf{G} as

$$\mathbf{G} \simeq \frac{R}{2\pi} \int_0^{2\pi} \int_{-\infty}^{+\infty} (\mathbf{r} \times \mathbf{v}) v'_r \rho dz d\phi, \quad (\text{C84})$$

$$= \frac{1}{2\pi} \Omega R^3 \int_0^{2\pi} \int_{-\infty}^{+\infty} \left(\hat{\mathbf{z}} - \frac{z}{R} \hat{\mathbf{R}} \right) v'_r \rho dz d\phi \quad (\text{C85})$$

where the unprimed and primed quantities refer to the background and perturbations. Inserting Equation (7) into (C86), we have

$$\mathbf{G} \simeq -\frac{1}{2\pi} \Omega^2 R^4 h \int_0^{2\pi} \int_{-\infty}^{+\infty} \frac{z^2}{R^2} [\text{Re}(U_r) \cos^2 \phi \hat{\mathbf{x}} + \text{Im}(U_r) \sin^2 \phi \hat{\mathbf{y}}] \rho dz d\phi \quad (\text{C86})$$

$$= -\frac{1}{2} \Sigma H R^3 \Omega^2 [\text{Re}(U_r), \text{Im}(U_r), 0] \quad (\text{C87})$$

which related complex U_r and vector \mathbf{G} .

D. DETAILS OF HYDRODYNAMIC SIMULATION SETUP

D.1. Grid and Boundary Conditions

Our simulations are preformed with Athena++ (Stone et al. 2020). We adopt spherical polar coordinates and uniformly spaced grid cells in r , θ and ϕ for our simulations. The azimuthal angle ϕ ranges from 0 to 2π while the radial r and polar θ coverages are given in Table 1. The ϕ domain is periodic; at each r and θ boundary of the domain, two ghost cells are attached outside the active mesh to implement boundary conditions.

The θ boundaries are placed sufficiently far from the disk midplane ($\geq 10H$ away from at $r = R_0$, $\geq 5.5H$ at $r = 1.5R_0$, and $\geq 2.5H$ at $r = 3.5R_0$) to ensure they do not influence the disk evolution. We impose reflective conditions, which are found to be the best for maintaining the vertical hydrostatic equilibrium of the disk and minimizing spurious inflows or outflows. Specifically, we copy the values of density ρ , radial velocity v_r , and azimuthal velocity v_ϕ from the last active cells into the ghosts, while the polar velocity v_θ is copied with its sign reversed. Similar boundary conditions have been used in a number of previous studies (e.g., Zhu 2019; Kimmig & Dullemond 2024).

The radial boundary condition needs to achieve two goals: (i) keeping the disk at fixed tilts, and (ii) allowing the gas flow to be consistent with steady viscous accretion. We denote quantities associated with the first/last active cells

with ' and those associated with the ghost cells with ". For (i), we hold the density values in the ghost cells at their initial values, i.e.,

$$\rho'' = \rho''(t=0). \quad (\text{D88})$$

For (ii), we set the velocity values in ghost cells in three steps: (1) calculate the cylindrical velocity components (v'_R, v'_ϕ, v'_z) with $\hat{\mathbf{z}}$ pointing at the direction of the disk plane (defined by $\beta = 0$ and $\beta = \beta_{\text{out}}$ at the inner and outer boundaries, respectively); (2) calculate these components for the ghost cells as

$$v''_R = v'_R \left(\frac{R''}{R'} \right)^{-1/2}, \quad (\text{D89})$$

$$v''_\phi = v'_\phi \left(\frac{R''}{R'} \right)^{-1/2}, \quad (\text{D90})$$

$$v''_z = 0; \quad (\text{D91})$$

then (3) convert them to the spherical-polar components ($v''_r, v''_\theta, v''_\phi$) and assign these values to the ghost cells.

D.2. Initial Condition and Tilting

The initial disk is set in two steps: first setting up a disk in its flat background state, and then applying a warp structure by tilting the disk. We use an initial background surface density profile

$$\Sigma(r) = \Sigma_0 r^{-3/2} \frac{1}{f_{\text{gap}}(r)}, \quad (\text{D92})$$

where

$$f_{\text{gap}}(r) = 1 + \frac{K-1}{2} \left[\tanh \left(\frac{r-R_a}{\Delta_a} \right) - \tanh \left(\frac{r-R_b}{\Delta_b} \right) \right] \quad (\text{D93})$$

controls the shape of the gap. The parameters R_a and R_b are the locations of the inner and outer gap edges, Δ_a and Δ_b are the steepness of the edges, and the constant K determines the depth of the gap. We use parameter values $(R_a, R_b, \Delta_a, \Delta_b, K) = (1, 2, 0.1, 0.2, 19)$ in all simulations. The background volume density ρ and Ω are set as in Appendix A.1.

To apply a tilting profile

$$\hat{\mathbf{t}} = [\sin(\beta) \cos(\gamma), \sin(\beta) \sin(\gamma), \cos(\beta)], \quad (\text{D94})$$

we rotate the fluid element at $\mathbf{r} = (r, \theta, \phi)$ to a new coordinate $\mathbf{r}' = (r, \theta', \phi')$ so that

$$\mathbf{r}' = \mathbf{R}_z(\gamma) \mathbf{R}_y(\beta) \mathbf{r}, \quad (\text{D95})$$

where $\mathbf{R}_z(\gamma)$ and $\mathbf{R}_y(\beta)$ are the standard 3D rotational matrices around the $\hat{\mathbf{z}}$ and $\hat{\mathbf{y}}$ axes, respectively. When we calculate \mathbf{r}' , we convert \mathbf{r} into cartesian coordinate so that apply $\mathbf{R}_z(\gamma)$ and $\mathbf{R}_y(\beta)$ can be applied; the resulting \mathbf{r}' is also in Cartesian coordinates, based on which we get spherical-polar coordinates (r, θ', ϕ') . As we rotate a fluid element from \mathbf{r} to \mathbf{r}' , we change its velocity vector to

$$\mathbf{v}' = \mathbf{R}_z(\gamma) \mathbf{R}_y(\beta) \mathbf{v} \quad (\text{D96})$$

and preserve its density ρ .

When we analyze a simulation, we can reverse this tilting procedure using the real-time measured β and γ . This allows us to map from the simulation coordinates \mathbf{r}_{sim} to the disk midplane coordinates \mathbf{r}_{disk} via

$$\mathbf{r}_{\text{disk}} = \mathbf{R}_y(-\beta) \mathbf{R}_z(-\gamma) \mathbf{r}_{\text{sim}}. \quad (\text{D97})$$

This is how we obtain the disk-plane snapshots in the right panels of Figure 5 and in Figure 12.

D.3. Viscosity

The public version of Athena++ applies constant kinematic viscosity ν by default. We implement the α viscosity prescription by manually enrolling a spatially varying ν in the problem generator.⁸

D.4. Integration Scheme

Local-Lax-Friedrichs method (LLF) is adopted to solve the hydrodynamic equations in our simulations, where the spatial reconstruction of the primitive fluid quantities is done using the piecewise Linear Method (PLM). We perform time integrations using the second-order accurate Runge-Kutta/Heun's method (RK2). All of the numerical methods here are already implemented in the public version of Athena++.⁹

At runtime, the simulation domains are typically divided into $4 \times 8 \times 13$ meshblocks in r , θ and ϕ directions, processed in parallel on 416 cores using MPI. Each simulation typically takes a 24 hours walltime to integrate for 150 code-unit time.

REFERENCES

- Benisty, M., Juhász, A., Facchini, S., et al. 2018, *A&A*, **619**, A171
- Benisty, M., Dominik, C., Follette, K., et al. 2023, in Astronomical Society of the Pacific Conference Series, Vol. 534, Protostars and Planets VII, ed. S. Inutsuka, Y. Aikawa, T. Muto, K. Tomida, & M. Tamura, 605, doi: 10.48550/arXiv.2203.09991
- Bohn, A. J., Benisty, M., Perraut, K., et al. 2022, *A&A*, **658**, A183
- Casassus, S., Marino, S., Pérez, S., et al. 2015, *ApJ*, **811**, 92
- Casassus, S., Avenhaus, H., Pérez, S., et al. 2018, *MNRAS*, **477**, 5104
- Deng, H., & Ogilvie, G. I. 2022, *MNRAS*, **512**, 6078
- Deng, H., Ogilvie, G. I., & Mayer, L. 2021, *MNRAS*, **500**, 4248
- Doğan, S., Nixon, C. J., King, A. R., & Pringle, J. E. 2018, *MNRAS*, **476**, 1519
- Dullemond, C. P., Kimmig, C. N., & Zanazzi, J. J. 2022, *MNRAS*, **511**, 2925
- Fairbairn, C. W. 2025, *ApJ*, **979**, 156
- Fairbairn, C. W., & Ogilvie, G. I. 2021a, *MNRAS*, **505**, 4906
- . 2021b, *MNRAS*, **508**, 2426
- Fairbairn, C. W., & Stone, J. M. 2025, arXiv e-prints, arXiv:2506.08839
- Foucart, F., & Lai, D. 2014, *MNRAS*, **445**, 1731
- Gammie, C. F., Goodman, J., & Ogilvie, G. I. 2000, *MNRAS*, **318**, 1005
- Held, L. E., & Ogilvie, G. I. 2024, *MNRAS*, **535**, 3108
- . 2025, arXiv e-prints, arXiv:2511.18655
- Kaaz, N., Liska, M. T. P., Jacquemin-Ide, J., et al. 2023, *ApJ*, **955**, 72
- Kaaz, N., Lithwick, Y., Liska, M., & Tchekhovskoy, A. 2025, *ApJ*, **979**, 192
- Keppler, M., Penzlin, A., Benisty, M., et al. 2020, *A&A*, **639**, A62
- Kimmig, C. N., & Dullemond, C. P. 2024, *A&A*, **689**, A45
- Kraus, S., Kreplin, A., Young, A. K., et al. 2020, *Science*, **369**, 1233
- Larwood, J. D., Nelson, R. P., Papaloizou, J. C. B., & Terquem, C. 1996, *MNRAS*, **282**, 597
- Liska, M., Hesp, C., Tchekhovskoy, A., et al. 2021, *MNRAS*, **507**, 983
- Lodato, G., & Price, D. J. 2010, *MNRAS*, **405**, 1212
- Lodato, G., & Pringle, J. E. 2007, *MNRAS*, **381**, 1287
- Lubow, S. H., & Ogilvie, G. I. 2000, *ApJ*, **538**, 326
- Marino, S., Perez, S., & Casassus, S. 2015, *ApJL*, **798**, L44
- Martin, R. G., Zhu, Z., & Armitage, P. J. 2020, *ApJL*, **898**, L26
- Muro-Arena, G. A., Benisty, M., Ginski, C., et al. 2020, *A&A*, **635**, A121
- Nixon, C., & King, A. 2016, in Lecture Notes in Physics, Berlin Springer Verlag, ed. F. Haardt, V. Gorini, U. Moschella, A. Treves, & M. Colpi, Vol. 905, 45, doi: 10.1007/978-3-319-19416-5_2
- Nixon, C., King, A., & Price, D. 2013, *MNRAS*, **434**, 1946
- Nixon, C., King, A., Price, D., & Frank, J. 2012, *ApJL*, **757**, L24
- Ogilvie, G. I. 1999, *MNRAS*, **304**, 557
- . 2008, *MNRAS*, **388**, 1372
- . 2018, *MNRAS*, **477**, 1744
- Ogilvie, G. I., & Latter, H. N. 2013a, *MNRAS*, **433**, 2403
- . 2013b, *MNRAS*, **433**, 2420

⁸ See details on Athena++'s discussion forum: <https://github.com/PrincetonUniversity/athena/discussions/411>.

⁹ We thank Dr. Alexander Dittmann for his suggestions on the integration scheme, which boost the numerical stability of our simulations.

- Paardekooper, S.-J., & Ogilvie, G. I. 2019, *MNRAS*, 483, 3738
- Panić, O., van Dishoeck, E. F., Hogerheijde, M. R., et al. 2010, *A&A*, 519, A110
- Papaloizou, J. C. B., & Lin, D. N. C. 1995, *ApJ*, 438, 841
- Papaloizou, J. C. B., & Pringle, J. E. 1983, *MNRAS*, 202, 1181
- Papaloizou, J. C. B., & Terquem, C. 1995, *MNRAS*, 274, 987
- Pineda, J. E., Quanz, S. P., Meru, F., et al. 2014, *ApJL*, 788, L34
- Pringle, J. E. 1992, *MNRAS*, 258, 811
- Rabago, I., Zhu, Z., Lubow, S., & Martin, R. G. 2024, *MNRAS*, 533, 360
- Raj, A., Nixon, C. J., & Doğan, S. 2021, *ApJ*, 909, 81
- Shakura, N. I., & Sunyaev, R. A. 1973, *A&A*, 24, 337
- Sorathia, K. A., Krolik, J. H., & Hawley, J. F. 2013, *ApJ*, 768, 133
- Stolker, T., Sitko, M., Lazareff, B., et al. 2017, *ApJ*, 849, 143
- Stone, J. M., Tomida, K., White, C. J., & Felker, K. G. 2020, *ApJS*, 249, 4
- Tanaka, H., Takeuchi, T., & Ward, W. R. 2002, *ApJ*, 565, 1257
- Winter, A. J., Benisty, M., Izquierdo, A. F., et al. 2025, *arXiv e-prints*, arXiv:2507.11669
- Zhu, Z. 2019, *MNRAS*, 483, 4221